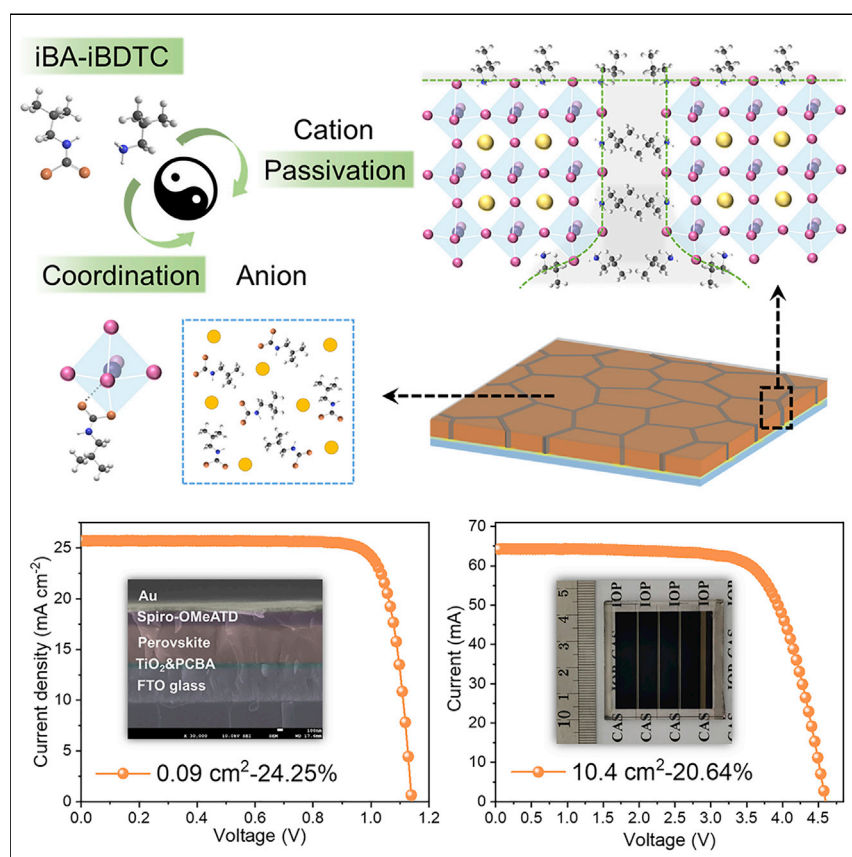


Article

Efficient, stable formamidinium-cesium perovskite solar cells and minimodules enabled by crystallization regulation



A dual-functional material comprising organic ammonium cation and dithiocarbamate anion is developed to regulate the crystallization and defects of the formamidinium-cesium perovskite. 24.25% efficiency in a single cell and >20.5% efficiency from a 10.4 cm² minimodule have been realized with excellent operational stability. Briefly, this exploitation of cation-anion synergistic effect from dual-functional additives provides more feasible technique routes for promoting the perovskite photovoltaic development and commercialization.

Yiming Li, Zijing Chen,
Bingcheng Yu, ..., Jiangjian Shi,
Dongmei Li, Qingbo Meng

shijj@iphy.ac.cn (J.S.)
dml@iphy.ac.cn (D.L.)
qbmeng@iphy.ac.cn (Q.M.)

Highlights

A dual-functional strategy is developed to regulate crystallization and defects

24.25% efficiency is achieved for a single PSC cell with excellent stability

>20.5% efficiency is realized from a 10.4 cm² minimodule

Article

Efficient, stable formamidinium-cesium perovskite solar cells and minimodules enabled by crystallization regulation

Yiming Li,^{1,3} Zijing Chen,^{1,5} Bingcheng Yu,^{1,3} Shan Tan,^{1,5} Yuqi Cui,^{1,5} Huijue Wu,¹ Yanhong Luo,^{1,4} Jiangjian Shi,^{1,*} Dongmei Li,^{1,4,*} and Qingbo Meng^{1,2,4,6,*}

SUMMARY

Formamidinium-cesium (FA-Cs) lead halide has attracted wide interest for enhancing the stability of perovskite solar cells; however, the crystallization of FA-Cs perovskite usually suffers from more complicated intermediate phase transition processes. Herein, we have developed a dual-functional additive consisting of organic ammonium cation and dithiocarbamate anion to regulate the crystallization and defects of the FA-Cs perovskite film. With a synergistic contribution of the cationic and anionic groups, 24.25% efficiency has been achieved in a single cell with excellent operational stability. Under steady-state light illumination and bias voltage, 90% power output of its initial state can still be obtained after 500 h of continuous operation. After enlarging the device from single cell to module, >20.5% efficiency has been realized from a 10.4 cm² minimodule by using only an ultralow-cost laser scribing technology. Briefly, this exploitation of cation-anion synergistic effect from dual-functional additives provides more opportunities for promoting the development of perovskite solar cells.

INTRODUCTION

Hybrid organic-inorganic perovskite materials have emerged as promising candidates for photovoltaics applications due to their outstanding optoelectronic properties and low-cost solution processing technique. Power conversion efficiency (PCE) of the perovskite solar cell (PSC) has rapidly risen over the last decade, from 3.8% to 25.5%, comparable with the crystal-Si technology.^{1,2} At present, the low stability and the efficiency loss under a cell area enlargement are two key issues that need to be overcome in the commercialization of PSCs.^{3–7} Recently, formamidinium-cesium (FA-Cs) lead halide perovskite has attracted wide interest because of its high thermal and operational stabilities.^{8,9} However, compared with the methylammonium perovskite, the crystallization of FA-Cs perovskite suffers from more complicated intermediate phase transition processes because the FA⁺ and Cs⁺ ion sizes mismatch, leading to smaller dipole moment and weaker interaction with the Pb-I framework.¹⁰ This has increased the difficulty of forming uniform perovskites, thus leading to the large lattice distortion, element segregation, and defect centers.

Crystallization regulation has been demonstrated as an effective approach to improve film quality and device performance of the PSC.¹¹ Perovskite crystallization usually starts from the Pb-I frameworks because they have already formed micro-nano nucleation centers in precursor solutions.^{12,13} As such, the regulation is mainly

Context & scale

Formamidinium-cesium (FA-Cs) lead halide has attracted a wide interest for stable perovskite solar cells (PSCs); however, the crystallization of FA-Cs perovskite usually suffers from complicated intermediate phase transition processes. Crystallization regulation using active coordination group to modify Pb-I frameworks has been demonstrated as an effective approach to improve the film quality and device performance. Surface, interface, and grain boundary defect passivation with organic long-chain ammonium halides is another necessary route for enhancing the cell performance and stability. Herein, a dual-functional material comprising organic ammonium cation and dithiocarbamate anion with the synergistic contribution of cationic passivation and anionic coordination effects is developed. This dual-functional strategy helps realize efficient and stable PSCs and minimodules and thus provides more opportunities for promoting the PSC development and commercialization.

realized through introducing additives or different solvent with more active coordination groups, which can modify the Pb-I cluster structure.^{14,15} Among them, the solvents having -S=O (i.e., dimethyl sulfoxide [DMSO]) or -C=O (i.e., N-methylpyrrolidinone [NMP]) have been widely exploited via forming solvent-PbI₂ adduct cluster to optimize the phase transition and crystallization of the perovskite.^{16,17} PbI₂·NMP-templated crystallization of FA-Cs perovskite has recently achieved a high PCE of 23% for small-area single cell and of over 20% for minimodule.¹⁸ Electron-donor anions such as COO⁻ and SCN⁻ have strong coordination ability with the Pb²⁺ and also played impressive roles in promoting the FA perovskite phase formation and device performance.^{19–21} With using MAHCOO (MA: methylammonium) ionic liquid solvent, black-phase FA perovskite has been stabilized at room temperature and high humidity with over 23% PCE.¹⁹ The small-area single-cell PCE has been further enhanced to over 25% by using FAHCOO additive.²⁰ Compared with the oxygen in HCOO⁻, sulfur has a much larger atom (or ion) radius and electron delocalization, which should be able to have more effective coordination with the Pb²⁺.²²

Besides coordination-induced crystallization regulation, surface, interface, and grain boundary defect passivation is another necessary route for enhancing the cell PCE and stability.^{23,24} Perovskite post-treatment with organic long-chain ammonium halides such as phenethylammonium iodide (PEAI), butylammonium iodide (BAI) or octylammonium iodide (OAI) has made a great contribution to the PCE enhancement of the cells.^{25–27} If the passivation effect of the long-chain ammonium cation and the coordination effect of the active anion can be synergistically realized, it will be a giant progress in simplifying processing complexity for highly efficient and stable PSCs.

Herein, we report efficient, stable PSCs and minimodules realized by using a dual-functional isobutylammonium isobutyldithiocarbamate (iBA-iBDTC) as an additive. CSS⁻ group of the iBA-iBDTC can effectively coordinate with the Pb²⁺ to improve the Pb-I nucleation and FA-Cs perovskite crystal growth. Additionally, the long-chain iBA⁺ cation group is distributed on the film surface and grain boundaries, passivating defects, reducing surface energy, and stabilizing surface structure. With the synergistic contribution of the cationic and anionic groups, the PCE of the small-area single cell has been improved to 24.25%, superior to the cell only using conventional isobutylammonium iodide (iBAI) passivation. The cell also exhibits excellent operational stability. Under steady-state light illumination and bias voltage (maximum power point [MPP] of the initial state), the cell can sustain 90% of its initial power output after 500 h of continuous operation. This dual-functional additive has also significantly enhanced the uniformity of the perovskite film to ensure high device performance when enlarging the cell area. Over 20.5% PCE has been achieved from a 10.4 cm² minimodule. Overall, the cation-anion synergistic effect of our dual-functional additive provides more feasible technique routes for promoting the PSC development and commercialization.

RESULTS

Device performance

The synthesized iBA-iBDTC comprises cation (CH₃)₂CHCH₂NH₃⁺ and anion (CH₃)₂CHCH₂NHCSS⁻, as shown in Figure 1A. The CSS⁻ is a dithiocarboxylate group obtained by the reaction of carbon disulfide with isobutylamine. The material product is confirmed by the ¹³C nuclear magnetic resonance (chemical shift peak at 212.81 ppm) and mass spectrometry (mass-to-charge ratio [m/z] peaks at about

¹Key Laboratory for Renewable Energy, Institute of Physics, Chinese Academy of Sciences, Beijing Key Laboratory for New Energy Materials and Devices, Beijing 100190, China

²Center of Materials Science and Optoelectronics Engineering, University of Chinese Academy of Sciences, Beijing 100049, China

³Huirou Division, Institute of Physics, Chinese Academy of Sciences, Beijing 101400, China

⁴Songshan Lake Materials Laboratory, Dongguan 523808, Guangdong, China

⁵School of Physics Science, University of Chinese Academy of Sciences, Beijing 100049, China

⁶Lead contact

*Correspondence: shijj@iphy.ac.cn (J.S.), dml@iphy.ac.cn (D.L.), qbmeng@iphy.ac.cn (Q.M.)

<https://doi.org/10.1016/j.joule.2022.02.003>

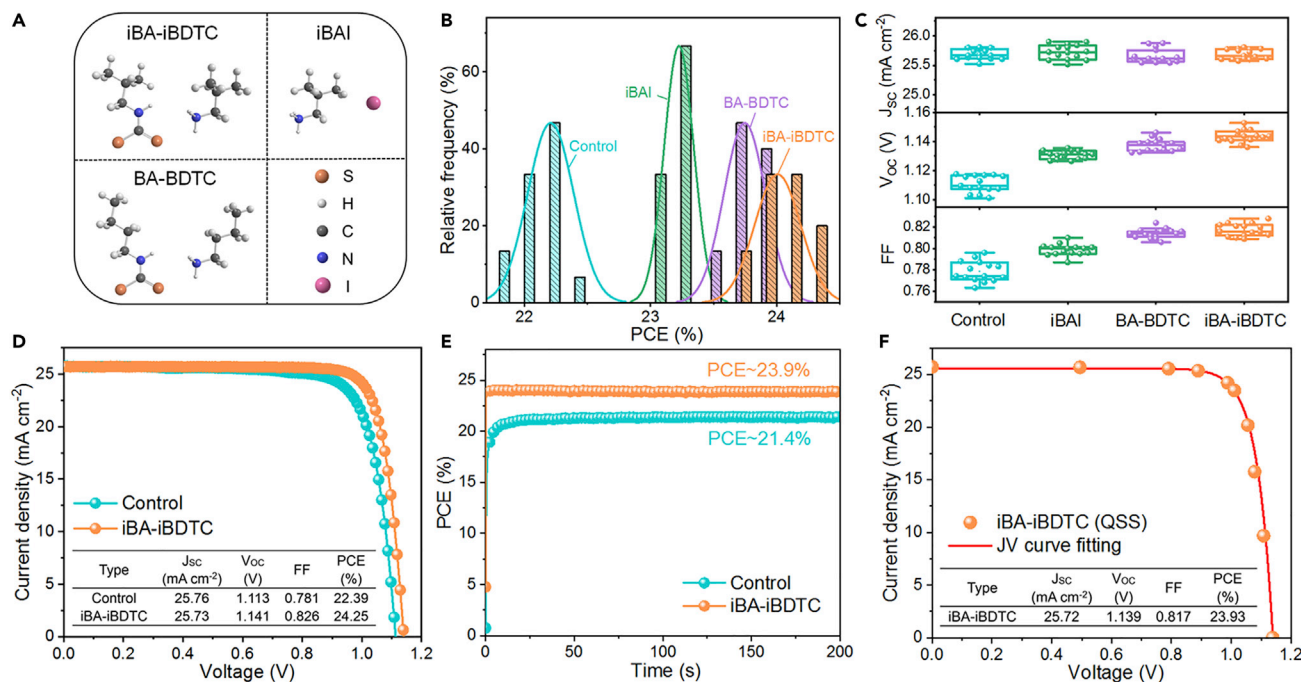


Figure 1. Device efficiency characterization

(A) Molecular structure of iBAI, BA-BDTC, and iBA-iBDTC.

(B) PCE distribution histograms of the cells with different modifications.

(C) Detailed performance parameters statistics.

(D) Current-voltage characteristic curves of the typical cells with or without the iBA-iBDTC modification.

(E) Steady-state power output of the control and modified cells for 200 s.

(F) Quasi-steady-state (QSS) measurement of the champion modified cell.

221.0, 149.0, and 73.9), as shown in Figures S1 and S2. For comparison, n-butylammonium butyldithiocarbamate (BA-BDTC) and conventional organic ammonium halide iBAI have also been synthesized and used here.

PSCs with a device configuration of FTO (F: SnO_2)/compact TiO_2 /fullerene derivative/perovskite/spiro-OMeTAD/Au (Figure S3) have been fabricated using these additives. Detailed experimental results regarding the additive concentration optimization and the additive introduction way are given in the supplemental information (Figures S4–S6). The PCE statistic histograms of these cells are shown in Figure 1B. The control cell exhibits an average PCE of 22.2%. When the iBAI was used, the average PCE is increased to 23.2%. Impressively, the introduction of BA-BDTC increases the average PCE to over 23.7% and the average PCE further reaches >24.0% when iBA-iBDTC is used. It is thus demonstrated the $-\text{CSS}^-$ anion has played an important role in improving the cell performance. The statistical distributions of short-circuit current density (J_{sc}), open-circuit voltage (V_{oc}), and fill factor (FF) of the cells are given in Figure 1C. It can be clearly seen that the higher PCE mainly benefits from V_{oc} and FF improvement, implying a significant enhancement in the perovskite quality.

Current-voltage (I - V) characteristics of the typical cells with or without the iBA-iBDTC modification are presented in Figure 1D. The modified cell exhibits a high PCE of 24.25% (forward scanned PCE: 23.41%) with J_{sc} of 25.73 mA cm^{-2} , V_{oc} of 1.141 V, and FF of 0.826, whereas the control cell has a PCE of 22.39% (forward scanned PCE: 20.30%) with J_{sc} of 25.76 mA cm^{-2} , V_{oc} of 1.113 V, and FF of 0.781 (Figure S7).

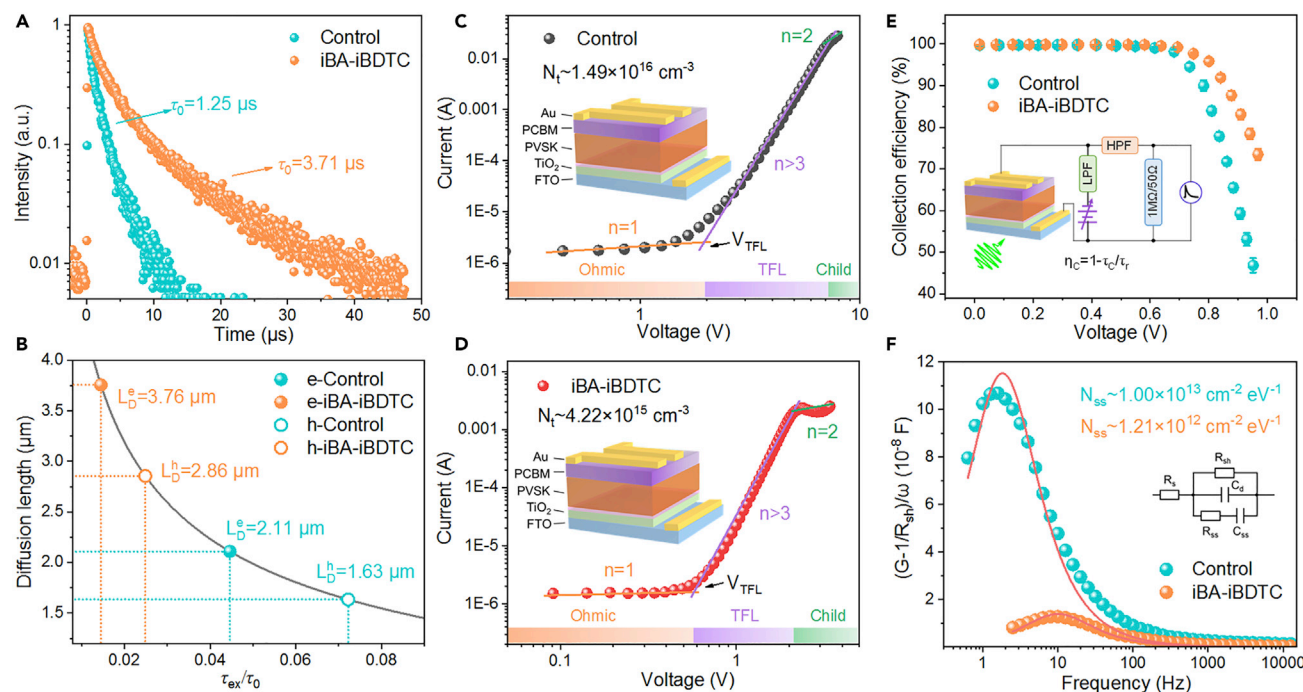


Figure 2. Defect characterization of perovskite films and devices

(A and B) (A) Time-resolved photoluminescence and (B) derived carrier diffusion length of perovskite films.

(C and D) Space charge limited current curves for electron-only devices (C. control perovskite and D. modified perovskite).

(E) Voltage-dependent charge collection efficiency (η_c) of the cells measured from modulated electrical transient measurements. Error bar: the standard deviation of measured samples.

(F) Interface defect extraction of the cells by using admittance measurement.

One of the modified cells has achieved a certified PCE of 23.7% (Figure S8). This cell performance has been among the highest results of the FA-Cs-based PSCs (Tables S1 and S2). Power output measurement of the modified cell for 200 s demonstrates a steady-state PCE of 23.9%; comparatively, the control cell only gives a maximum PCE of 21.4%. We also conducted quasi-steady-state (QSS) I - V measurement of the champion cell after the I - V scanning, and the result is shown in Figures 1F and S11. The current of the cell under a fixed voltage was recorded when the current fluctuation is $<0.1\%$. The QSS- I - V gives a PCE of 23.93% with J_{SC} of 25.72 mA cm^{-2} , V_{OC} of 1.139 V and FF of 0.817. External quantum efficiency (EQE) spectrum of the modified cell has also been measured (see Figures S9 and S10). EQE of $>90\%$ can be achieved over a wide wavelength range from 410 to 740 nm, which finally gives an integral J_{SC} of about 25.15 mA cm^{-2} , agreeing well with the I - V result.

We use optical and electrical characterization to study defect of the perovskite films with and without the iBA-iBDTC modification because it is the most important physics properties that influence the cell performance. From time-resolved photoluminescence (Figure S14), it is found that the charge non-radiative recombination lifetime of the modified film exhibits a three-fold enhancement (Figure 2A). This helps to improve carrier diffusion length of the perovskite film by about two times (Figure 2B), indicating the defect induced charge loss is suppressed when the cell works.²⁸ Defect density of the film is further measured by using the space charge limited current (SCLC) method on an electron-only device, as depicted in Figures 2C and 2D).²⁹ With modification, the trap filled limit voltage (V_{TFL}) of the device

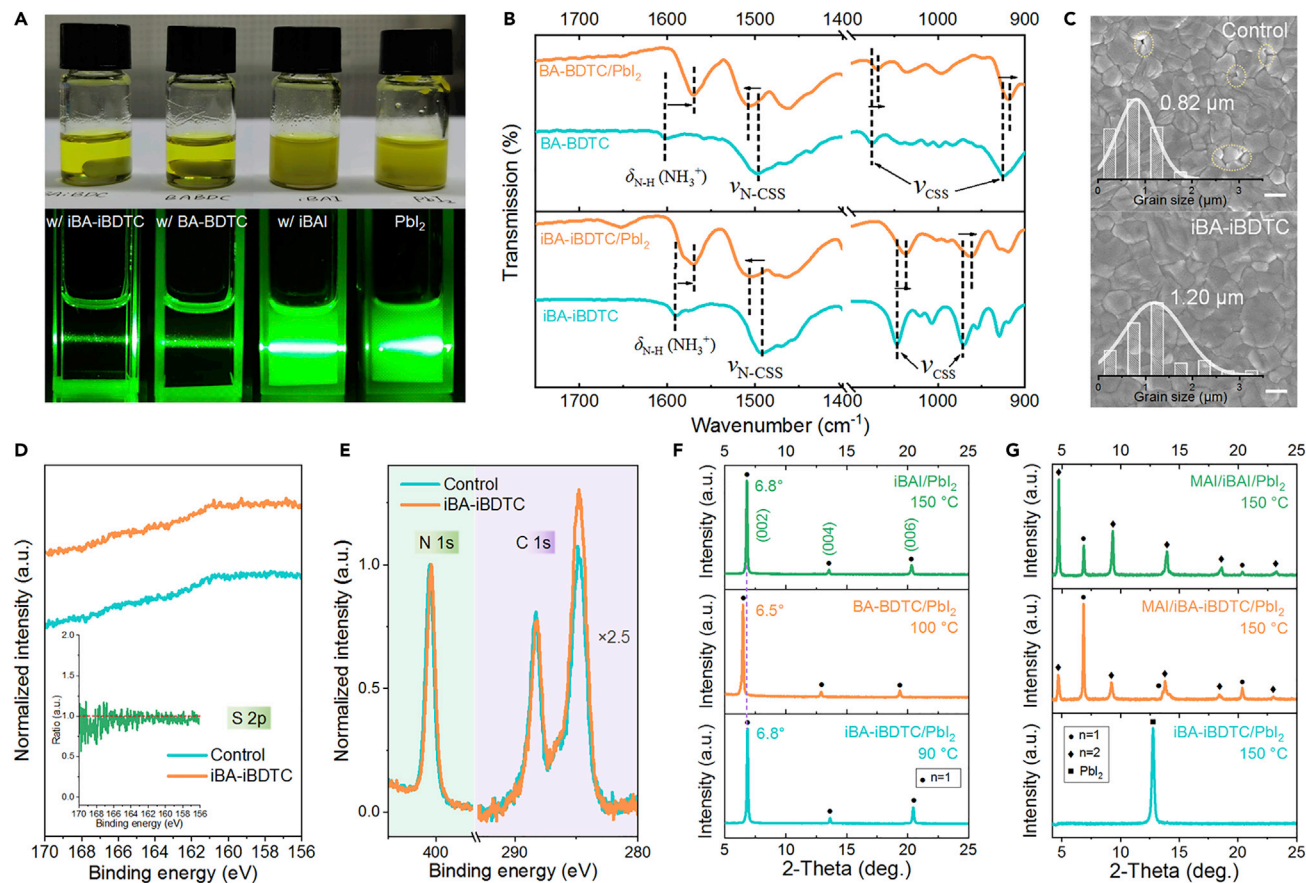


Figure 3. Interaction between -CSS- anionic group and Pb-I framework

(A) Tyndall effect of PbI_2 solutions in *N,N*-Dimethylformamide with different additives.

(B) Fourier transform infrared spectra of the iBA-iBDTC and BA-BDTC before and after mixing with PbI_2 , respectively.

(C) Scanning electron microscopy images of perovskite films. Scale bar: 1 μm . The inset presents corresponding grain size distribution.

(D and E) X-ray photoelectron spectroscopy (XPS) results of S 2p (D), N 1s, and C 1s (E) for perovskite films. The inset in (D) is the ratio between the two XPS spectra.

(F and G) X-ray diffraction (XRD) patterns of PbI_2 when reacted with iBA-iBDTC, BA-BDTC, and iBAI under different conditions.

has been decreased from 2 to <0.6 V, indicating a 3.5-fold reduction in the defect density, from 1.49×10^{16} to $4.22 \times 10^{15} \text{ cm}^{-3}$. Charge loss of the cell that directly correlates to the photoelectrical conversion process, has been studied by using an electrical transient method.³⁰ Modulated transient photocurrent and photovoltage of these cells are measured and their decay time is used for calculating the charge collection efficiency (η_c). As in Figure 2E, at a voltage of >0.8 V, η_c of the modified cell is obviously higher than that of the control cell. This improvement in the η_c is the direct reason for the V_{OC} increase of the cell. Interface defect density (N_{SS}) is particularly characterized by using an admittance method, as in Figure 2F,³¹ and an eight-fold reduction in the N_{SS} has been observed for the modified device, indicating an obvious interface modification effect exists in the iBA-iBDTC device.

Mechanism discussion

To uncover the role of the iBA-iBDTC, we have further conducted material and chemistry mechanism studies. Tyndall effect experiment based on light-colloid scattering has been firstly carried out to evaluate possible interactions between CSS^-

and Pb-I clusters (Figures 3A and S15). As in Figure 3A, dissolving 1 M PbI_2 in N,N-dimethylformamide (DMF) results in a turbid solution with strong but disordered light scattering, indicating the existence of numerous Pb-I clusters with varied sizes.^{12,13} These clusters usually perform as initial nucleation centers in the perovskite deposition process and will influence uniformity of the final film.³² Currently, it has been widely recognized that decreasing the Pb-I cluster size and disordering degree is necessary for optimizing the perovskite nucleation to facilitate the uniform incorporation of FA and Cs into the Pb-I framework during the nucleation and crystal growth process.¹⁸ This purpose has been well realized by adding iBA-iBDTC or BA-BDTC into the PbI_2 solution, as indicated by the clear solution and much weaker light scattering. In contrast, no such effect can be achieved by using the iBAI additive. This means that long-chain organic ammonium, such as iBA^+ , cannot modify the Pb-I framework in solution, and moreover, CSS^- anion has a much stronger interaction with the Pb^{2+} compared with the I^- anion.

This interaction has been further verified by using Fourier transform infrared spectroscopy (FTIR), as presented in Figure 3B. Symmetrical and asymmetric stretching vibrations of CSS^- (ν_{CSS}) in iBA-iBDTC can be seen at 972 and 1,046 cm^{-1} , respectively. N-H bending vibration of the NH_3^+ [$\delta_{\text{N-H}}(\text{NH}_3^+)$] appears at 1,591 cm^{-1} and the N-CSS stretching vibration ($\nu_{\text{N-CSS}}$) can be seen at 1,491 cm^{-1} . When mixing with the PbI_2 , this peak is shifted due to the interaction between CSS^- and Pb^{2+} . $\delta_{\text{N-H}}(\text{NH}_3^+)$ peak is red-shifted by $\sim 22 \text{ cm}^{-1}$, indicating that the initial interaction between NH_3^+ and CSS^- in the iBA-iBDTC disappears. ν_{CSS} peak is shifted to a lower wavenumber position by $\sim 9 \text{ cm}^{-1}$, implying that a stronger coordination interaction between the CSS^- and Pb^{2+} group has formed. $\nu_{\text{N-CSS}}$ peak is also shifted to higher wavenumber position. Similar FTIR peak signatures are found for the interaction between BA-BDTC and PbI_2 . With the iBA-iBDTC modification, nucleation and crystal growth of the perovskite film have been improved with larger grains and denser smoother surface (Figures 3C and S16). X-ray photoemission spectroscopy (XPS) has been employed to study the surface chemistry properties of the perovskite film (Figures 3D, 3E, and S17). It is interesting to find that no sulfur element exists on the modified film surface (Figure 3D), and similar conclusion is also obtained in the bulk film by using Ar^+ -assisted XPS measurement (Figure S18), implying that the iBDTC⁻ anion is completely removed after the annealing process. Differently, C/N elemental ratio on the film surface has been obviously increased after the iBA-iBDTC modification (Figure 3E), confirming that some iBA^+ cation has been retained. Besides, only one N 1s peak centered at $\sim 400.5 \text{ eV}$ assigned to FA^+ is found, whereas no extra shoulder peak at $\sim 402.5 \text{ eV}$ corresponding to the MA^+ can be detectable although methylammonium chloride (MACl) was used as an additive. Even so, we need to note that, it is really difficult to completely rule out the possibility that a little MA may insert into the perovskite lattice through the FA/MA cation exchange. The MA may have played an important role in helping to remove the iBDTC⁻ while retaining the iBA^+ . In high-temperature annealing process, MA^+ and iBDTC⁻ can synergistically volatilize by forming volatile CH_3NH_2 and $(\text{CH}_3)_2\text{CHCH}_2\text{NHCSSH}$. This process has been further tracking by X-ray diffraction (XRD) of the reaction between iBA-iBDTC and PbI_2 under different conditions (Figures 3F, 3G, S19, and S20). At low annealing temperature, the reaction between PbI_2 and iBA-iBDTC (or BA-BDTC) can form a two-dimensional perovskite structure, similar to the iBAI/ PbI_2 reaction. At relatively high temperature of 150°C, no iBA-iBDTC can be retained in the iBA-iBDTC/ PbI_2 mixed system because of thermal decomposition of iBA-iBDTC. However, when MAI is introduced, two-dimensional type perovskite structure can still be formed, implying that the synergistic volatilization of MA-iBDTC

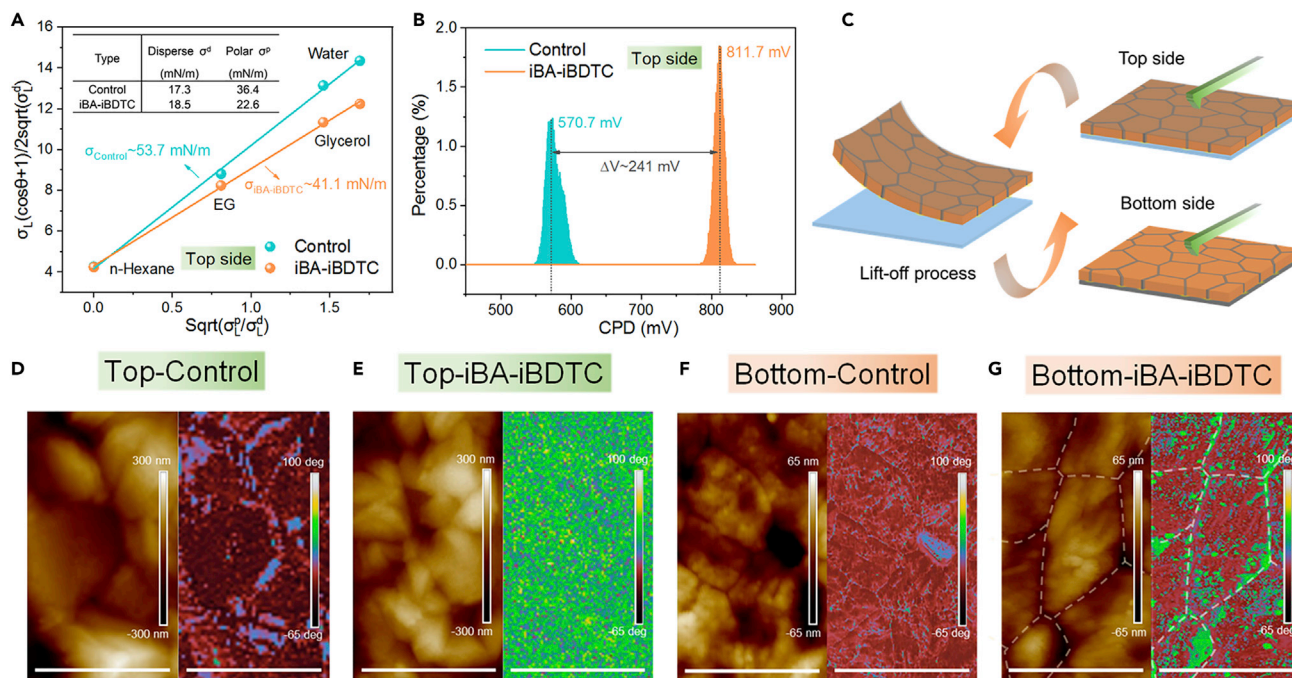


Figure 4. Spatial distribution of the iBA⁺ cationic passivation layer in the perovskite film

(A) Surface tension measurement of perovskite films with and without the iBA-iBDTC modification using the OWRK method. (B) Surface contacting potential difference (CPD) distribution of perovskite films measured by Kelvin probe force microscopy (KPFM). (C) Schematic illustration of the film lift-off process for atomic force microscopy (AFM) measurement of both the top and bottom surfaces. (D–G) AFM morphology and corresponding phase images of top and bottom surfaces (D, top surface of control film, E, top surface of modified film, F, bottom surface of control film, and G, bottom surface of modified film). Scale bar: 1 μ m.

could help to stabilize the iBA⁺ at the high temperature. Stabilizing the iBA⁺ in the film is the key to realize surface passivation.

We performed surface tension measurement to investigate the influence of iBA⁺ cation on the perovskite film, which was realized by using the Owens-Wendt-Rabel-Kaelble (OWRK) method.³³ Contacting angles (θ) of four types of liquids on the perovskite film surface were measured; the relationship between the θ and the tension properties of these liquid gives the surface tension of the perovskite film (Figures S22 and S23; Table S3). As shown in Figure 4A, the polar component (σ^p) of the surface tension has been obviously decreased from 36.4 to 22.6 mN m⁻¹. Notably, σ^p of the control perovskite has a similar value to that of a FA-MA-based perovskite measured in our previous work.³⁴ This implies that unmodified perovskite is usually terminated with Pb-I surface and the +1 valent cations, such as FA, MA, and Cs, are deficient there and thus have little influence on the surface properties. The σ^p reduction here means that the perovskite surface dipole polarity has been effectively decreased by the introduction of the -CH(CH₃)₂ terminal group. Decreasing the surface tension is beneficial for stabilizing the surface atomic or molecular structure, as also indicated by the in-situ contacting angle characterization. Contacting potential difference (CPD) obtained from the Kelvin probe force microscopy (KPFM) also demonstrates that the surface electrical properties of the perovskite has been changed by the iBA⁺ incorporation, with higher CPD and more uniform potential distribution (Figures 4B and S21).

To further probe the iBA⁺, we use atomic force microscopy (AFM) to characterize phase distribution properties of both the top and bottom surfaces of the perovskite film. A film lift-off process was applied to expose and uncover the buried

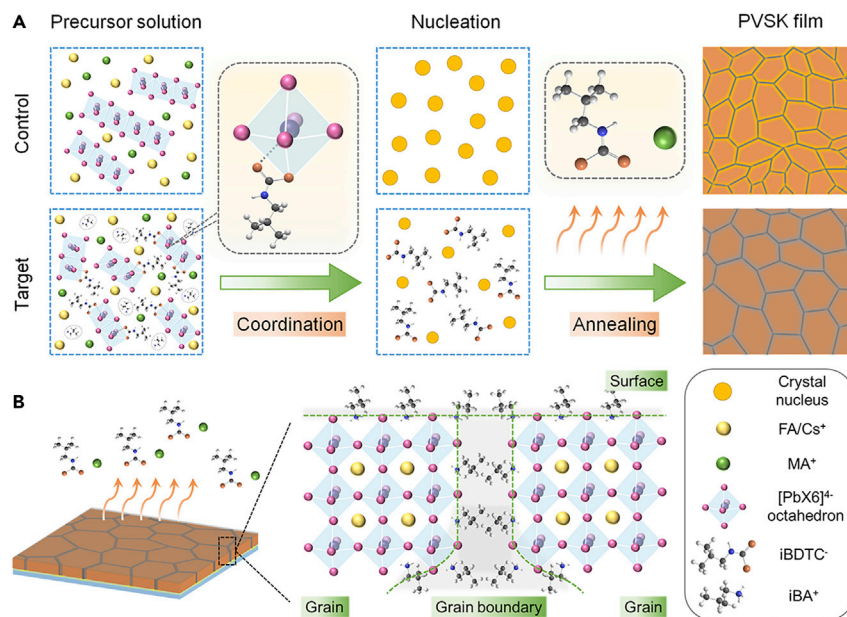


Figure 5. Schematic illustration of the material and chemistry mechanism for regulating the crystallization and defect of the perovskite film by using iBA-iBDTC

(A) Interaction between -CSS^- group and Pb-I framework and the influence on nucleation and crystal growth of perovskite film.

(B) Spatial distribution of the iBA^+ passivation layer in the perovskite film.

bottom surface (Figure 4C, scheme).³⁵ For these two surfaces, besides the morphology, difference in the AFM phase distribution can be clearly seen (Figures 4D–4G). AFM phase distribution of the top surface of the control film is mainly located at -33° ; for the modified film, the AFM phase has been significantly increased to 30° and no signatures of the grain boundary can be observed. This indicates that the film surface has been uniformly covered with an iBA^+ layer that has different mechanical properties to the Pb-I-terminated perovskite. For the bottom surface of the control film, the AFM phase is slightly increased to -25° with negligible grain boundary signatures, implying that both the top and bottom surface of the pristine perovskite has similar composition and mechanical properties; for the modified film, its internal grains have similar AFM phase to the control perovskite, whereas its grain boundaries have AFM phase at about 27° , almost the same as that of the top surface. This result means that the iBA^+ was deeply inserted into the grain boundaries of the perovskite film, reaching the bottom surface and distributing around the grain boundaries. As such, high defective area of the perovskite film, that is, the surface and grain boundary, has been fully passivated by using the iBA-iBDTC additive.

Material and chemistry mechanism for regulating the perovskite crystallization and defect by using iBA-iBDTC is schematically illustrated in Figure 5. Through interaction between -CSS^- group and Pb-I framework, large-size Pb-I structures in the precursor film are broken down. The resulting low-density nucleation centers will facilitate the crystal growth of the perovskite film. After that, the iBDTC^- anion is removed through thermal decomposition and synergistic volatilization with MA. For the retained iBA^+ cation, the -NH_3^+ terminal group will incorporate into the interval of surface Pb-I octahedrons and uniformly distribute on the film surface and grain boundaries for realizing passivation effect.

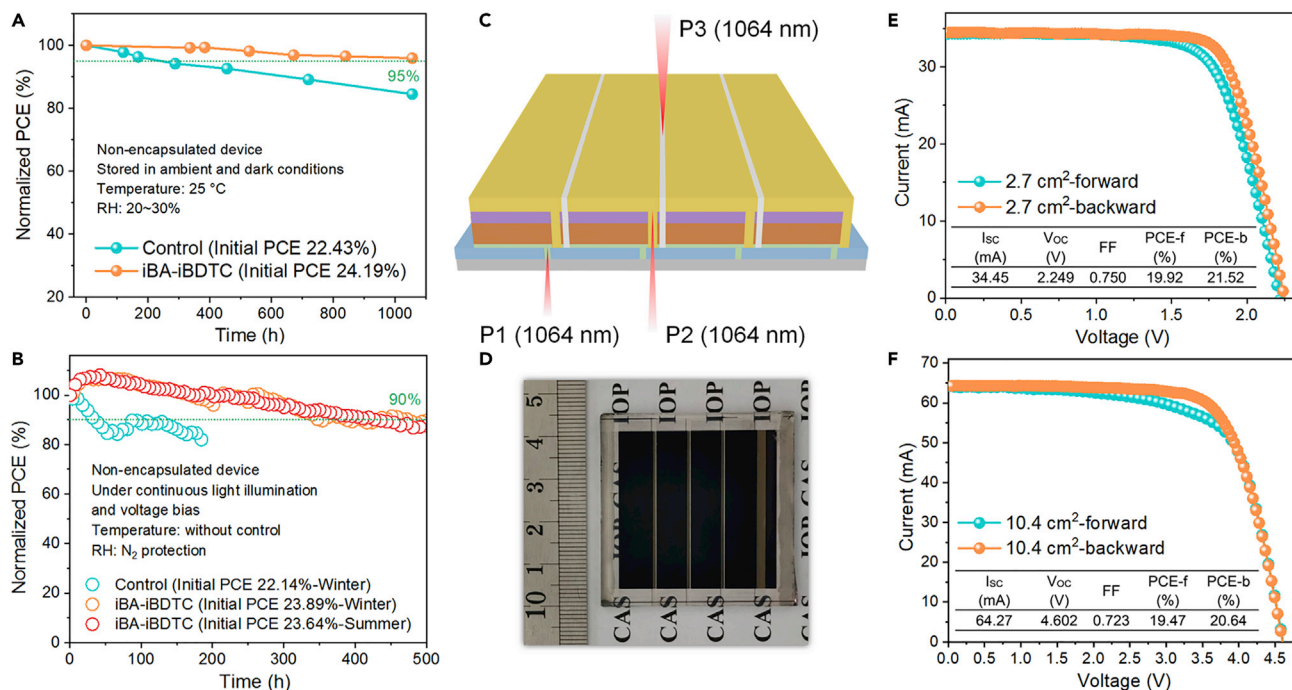


Figure 6. Stability and large-area device performance

(A) PCE tracking of non-encapsulated cells stored in ambient conditions (temperature: 25°C, relative humidity: 20%~30%) for 1000 h. (B) Operational stability tracking of cells under steady-state light illumination and bias voltage for 500 h (N₂ atmosphere, white LED, and uncontrolled temperature). (C) Schematic diagram of fabrication of a minimodule comprising four series-connected sub-cells. The P1-P3 scribing is realized using a supercheap fiber laser (1,064 nm). (D) Photograph of a minimodule fabricated on 4.5 × 4.5 cm² glass substrate. (E and F) I-V characteristics of best performed 2.7 cm² (E) and 10.4 cm² minimodules (F).

Stability and minimodules

Stability performance of the cells are investigated under different aging conditions. When stored in ambient conditions (temperature: 25°C, relative humidity: 20%~30%) after 1,000 h, the iBA-iBDTC modification helped the non-encapsulated cell to retain >95% of its initial PCE (Figure 6A). Detailed parameter variation of these cells is shown in Figures S24–S26. Operational stability is further evaluated by keeping the cell working under continuous light illumination and steady-state bias voltage (MPP of the initial state) without controlling the cell temperature. After 500 h operation, the modified cell can still provide 90% power output of its initial state (Figure 6B). Comparatively, PCE of the control cell has already exhibited fast decline in the first 100 h. This demonstrates that besides efficiency, the iBA-iBDTC modification makes a considerable contribution in enhancing the cell stability.

Based on the excellent single-cell performance, we have further attempted to enlarge the device area by fabricating minimodules on large-size substrate. Using a conventional series-connected structure, 4.5 × 4.5 cm² minimodules comprising four sub-cells were fabricated based on the spin coating method. The fabrication process is schematically shown in Figure 6C. Here, inspired by previous work,³⁶ the P1-P3 is realized using a supercheap fiber laser (1,064 nm) with galvo scanning. In P2 and P3 steps, laser focus point is set several millimeters beneath the scribed surface (i.e., perovskite and Au film) to eliminate the damage to the FTO layer that is ultrasensitive to the 1,064 nm laser. Photograph of the minimodule is shown in

Figure 6D, which has an active area of 10.4 cm². Figure 6E firstly shows the *I*-*V* characteristics of a two sub-cell minimodule with an active area of 2.7 cm², which gives a backward scanned PCE of 21.52% (forward PCE: 19.92%). In the four sub-cell minimodule (Figures 6F and S27), a champion backward scanned PCE of 20.64% can be achieved (forward PCE: 19.47%). This indicates that iBA-iBDTC-modified perovskite films indeed exhibit excellent photovoltaic performance. However, compared with the single cell, FF reduction is the main factor to influence the module PCE. If the laser scribing process could be further improved, we believe higher device performance will be obtained in the future. Nevertheless, the PCE of >20.5% has been among the highest results of the perovskite minimodule (>10 cm²), and thus brings more technique opportunities for achieve high performance PSC with low-cost processes.

DISCUSSION

In this work, we have realized efficient and stable PSC and minimodule by using the iBA-iBDTC to regulate the crystallization and defect of the perovskite film. With the synergistic contribution of the cationic and anionic groups from the iBA-iBDTC, 24.25% PCE (certified PCE: 23.7%) has been achieved in the single PSCs. This has been among the highest results of FA-Cs based PSCs, much superior to the cell only using conventional iBAI passivation. The cell also exhibits excellent operational stability. Under steady-state light illumination and bias voltage, the cell can still provide 90% power output of its initial state after 500 h of continuous operation. After enlarging the device from single cell to module, >20.5% PCE has been achieved from a 10.4 cm² minimodule when only using an ultralow-cost laser scribing process technology. Overall, the exploitation of cation-anion synergistic effect of these dual-functional additives provides more opportunities for promoting the PSC development and commercialization.

EXPERIMENTAL PROCEDURES

Resource availability

Lead contact

Further information and requests for resources and materials should be directed to and will be fulfilled by the lead contact, Qingbo Meng (qbmeng@iphy.ac.cn).

Materials availability

This study did not generate new unique materials.

Data and code availability

This study did not generate or analyze (datasets or code).

Reagents and materials

PbI₂ (99.99%), formamidinium iodide (FAI, 99.5%), formamidinium bromide (FABr, 99.5%) and methylammonium chloride (MACl, 99.5%) were purchased from Xi'an Polymer Light Technology Corp. CsI (99.9%) was obtained from Aldrich. N,N-dimethylformamide (DMF, 99.8%), dimethyl sulphoxide (DMSO, 99.8%), chlorobenzene (CB, 99.9%), and polystyrene (PS) were from Alfa Aesar. Trimethylphenylammonium iodide (TPAI, 99%), n-butylamine (BA, 99.5%), isobutylamine (iBA, 99.5%) and carbon disulfide (CS₂, 99.9%) were purchased from Aladdin. n-hexane (98%) was from Innochem. Ethanol (AR) and chloroform (AR) were from Beijing Tong Guang Fine Chemicals Company. 4-tert-butylpyridine (TBP) and bis(trifluoromethane) sulfonimide lithium salt (LiTFSI) were purchased from Sigma-Aldrich, and spiro-OMeTAD was obtained from Luminescence Technology Corp. Tris(2-(1H-pyrazol-1-yl)-4-tert-butylpyridine)-cobalt(III) tris(bis(trifluoromethylsulfonyl)imide) (FK209) was from

Dyesol. All the chemicals were directly used without further purification. Laser-patterned FTO glass (sheet resistance of $8.5 \Omega \text{ sq}^{-1}$) was sequentially cleaned with a mild detergent, alkali liquor, distilled water, and ethanol in an ultrasonic bath. The substrate was treated with ozone for 30 min prior to use.

Synthesis of isobutylammonium dithiocarbamate salt (iBA-iBDTC)

500 μL CS_2 and 1,700 μL iBA were put into a round bottom flask and mixed in 5 mL ethanol. The mixture was stirred in ice bath for 2 days. Then, 1 mL n-hexane was added, then centrifugated to afford white solid product. The crude product was recrystallized in ethanol/n-hexane for three times. The final product is white powder with $\sim 85\%$ yield.

iBA-iBDTC: ^1H NMR (500 MHz, CD_3OD): 0.96 (d, 6H), 1.04 (d, 6H), 2.04 (m, 2H), 2.86 (d, 1H), 3.33 (s, 1H), 3.39 (d, 2H), 4.96 (s, 4H); ^{13}C NMR (600 MHz, CD_3OD): 212.81 (s, 1C), 55.01 (s, 2C-N), 47.25–47.98 (m, 2CH), 27.67 (s, 1 CH_2), 26.93 (s, 1 CH_2), 19.25 (s, 2 CH_3), 18.74 (s, 2 CH_3). HRMS-MALDI-TOF calcd for $\text{C}_5\text{H}_{10}\text{NS}_2^-$ and $\text{C}_4\text{H}_{12}\text{N}^+$: 148.1917 and 74.0507, respectively. Found: 149.03285 and 73.92001.

Perovskite film deposition and device fabrication

Precursor solution for perovskite films was prepared by dissolving 1.736 M PbI_2 , 1.600 M FAI, 0.048 M FABr, 0.048 M CsI and 0.533 M MAI in DMF/DMSO mixed solvent (v: v = 8.5: 1.5). The precursor solution was stirred for 5 h at room temperature and was filtered before use. The compact TiO_2 layer was deposited on the FTO glass with a 0.125 M titanium isopropoxide sol-gel precursor solution by spin coating at 3,000 rpm for 30 s, then sintered at 500°C for 1 h. The TiO_2 film was subsequently treated with 0.025 M TiCl_4 aqueous solution for 35 min, and sintered at 500°C for 1 h. [6,6]-phenyl-C61-butyric acid (PCBA, 0.2 mg/mL) and 1.5 mg/mL PS in CB was spin-coated on the top of TiO_2 films. Perovskite films were fabricated by anti-solvent single-step spin-coating method. In details, the perovskite precursor solution was spin-coated at 1,000 rpm for 10 s and 5,000 rpm for 30 s, CB (120 μL) was poured onto the substrate at 15 s during the high speed stage. For iBA-iBDTC, iBAI and BA-BDTC treated perovskite films, different concentrations of iBA-iBDTC, iBAI and BA-BDTC were dissolved in perovskite precursor solution, anti-solvent CB, or post-treatment chloroform, respectively. The half-crystallization film was heated at 150°C for 10 min in dry air (RH: 20%~30%). After cooling down, 1.3 mg/mL of TPAI in chloroform was spin-coated at 3,000 rpm to passivate the surface of perovskite films. A 200 nm-thick spiro-OMeTAD layer was deposited on the top of perovskite films by spin-coating at 3,000 rpm for 30 s, then heated at 60°C for 10 min. Spiro-OMeTAD solution was prepared by following the literature. For SCLC devices, 20 mg/mL PCBM in CB was spin-coated on the top of perovskite films at 1,000 rpm for 30 s and then heated at 60°C for 10 min. Finally, 80 nm thick Au electrodes were deposited via thermal evaporation at an atmospheric pressure of 10^{-7} Torr (Kurt J. Lesker). In all the cell fabrication processes, strictly controlling the quality of perovskite raw materials and carefully optimizing the experimental environments of TiO_2 , PCBA/PS interface layer and perovskite layer depositions are always necessary for obtaining low-hysteresis solar cells.

Characterizations

If without special noting, all the measurements were carried in ambient conditions (temperature: 25°C , relative humidity: 20%~30%). Current-voltage (I-V) characteristics were measured under AM 1.5 simulated sunlight (100 mW cm^{-2}) from Zolix

SS150A after spectral mismatch correction, which was recorded by a digital source meter (Keithley model 2602). The light intensity for the *I*-*V* measurements was calibrated (see [Figure S12](#)) with a reference silicon cell (provided and certified by the National Institute of Metrology, China (NIM, China) at September 3th, 2019). The small-area solar cells were masked with a black mask to determine an aperture of 0.08912 cm² (certified by National Institute of Metrology, China) and the area with Au back contact is 0.162 cm². The scanning speed was 50 mV s⁻¹ with a delay time of 0.3 s ([Figure S13](#)). The scanning range is from -50 to 1,200 mV (forward) or from 1,200 to -50 mV (backward). To reduce the hysteresis, the relative humidity of the *I*-*V* measurement environment has been reduced to below 15%. The QSS-*I*-*V* measurement is conducted with the same instrument. Voltage at the cell is fixed by the source meter and the QSS current is continuously traced. The QSS *V*_{OC} is recorded by a digital voltage meter (fluke 8808A) when it reaches a stabilized value. The EQE spectra were performed by using Enli Technology (Taiwan) EQE system, which was calibrated with a crystalline silicon photovoltaic cell before use. Antireflection coating was used for device performance characterizations, and the corresponding transmittance spectra were given in [Figure S10](#). Steady state and time-resolved transient photoluminescence (PL) spectra were conducted on an Edinburgh fluorescence spectrometer (FLS 920). A 638.2 nm pulsed diode laser (EPL-640, ~4 mW cm⁻², 62 ps, 20 MHz) was used as the excitation source. Modulated transient photocurrent and photovoltage (m-TPC/TPV) measurements were obtained by a tunable nanosecond laser (Opotek, RADIANT 532 LD) pumped at 532 nm and recorded by a sub-nanosecond resolved digital oscilloscope (Tektronix, MDO3034) with input impedances of 50 Ω or 1 MΩ, respectively. A signal generator (Tektronix, AFG3052C) together with a low-pass filter was applied to give steady-state bias voltages over the cell. The admittance spectroscopy was conducted on VersaSTAT 3 Electrochemical Workstation of Princeton Applied Research in the dark from 0.1 to 10⁶ Hz with 10 mV amplitude and the DC bias was kept at zero. Fourier transform infrared spectra (FTIR) were performed on TENSOR 27 spectrometer, Bruker. The morphology of the samples was observed by using a scanning electron microscope (SEM) from Zeiss Sigma 300. XPS measurement was carried out on an ESCALAB 250Xi (Thermo Fisher) instrument. XRD patterns were measured on a Bruker X-ray diffractometer using Cu Kα as the radiation source. Contact angles were obtained by OCA25, DataPhysics. AFM images and KPFM image were carried out on MultiMode 8 SPM. UV-vis absorption spectra were measured on Shimadzu UV-2550. HRMS-MALDI-TOF was obtained on APEX II FT-ICR-MS. ¹H NMR data (CD₃OD) was obtained on Bruker Avance III 500WB and ¹³C NMR data were from Bruker Neo 600.

SUPPLEMENTAL INFORMATION

Supplemental information can be found online at <https://doi.org/10.1016/j.joule.2022.02.003>.

ACKNOWLEDGMENTS

This work was supported by Natural Science Foundation of China (No. 51872321, 11874402, 52172260, 52072402, 52102332, 51627803). The authors would like to thank Dr. Jiangyang Shao for his kind help for MS measurement.

AUTHOR CONTRIBUTIONS

Y. Li, J.S., D.L., and Q.M. conceived the idea. Y. Li did experimental designs, device fabrication, and data analysis. Z.C., B.Y., S.T., and Y.C. participated in the device fabrications and some material and device characterizations.

D.L., Y. Luo, and H.W. supported the measurement system construction, device fabrication, characterization, and discussions. Y. Li, J.S., D.L., and Q.M. participated in manuscript writing and revising. J.S. and D.L. polished the manuscript language. All authors were involved in the discussions and approved the manuscript.

DECLARATION OF INTERESTS

The authors declare no competing interests.

Received: August 27, 2021

Revised: October 18, 2021

Accepted: February 4, 2022

Published: March 1, 2022

REFERENCES

- Kojima, A., Teshima, K., Shirai, Y., and Miyasaka, T. (2009). Organometal halide perovskites as visible-light sensitizers for photovoltaic cells. *J. Am. Chem. Soc.* *131*, 6050–6051.
- NREL National Center for Photovoltaics (2021). Best research-cell efficiency chart. <https://www.nrel.gov/pv/cell-efficiency.html>.
- Li, N., Niu, X., Chen, Q., and Zhou, H. (2020). Towards commercialization: the operational stability of perovskite solar cells. *Chem. Soc. Rev.* *49*, 8235–8286.
- Shi, J., Li, Y., Li, D., Luo, Y., Wu, H., and Meng, Q. (2018). From ultrafast to ultraslow: Charge-Carrier dynamics of perovskite solar cells. *Joule* *2*, 879–901.
- Davies, M.L. (2020). Addressing the stability of lead halide perovskites. *Joule* *4*, 1626–1627.
- Ono, L.K., Qi, Y., and Liu, S.F. (2018). Progress toward stable lead halide perovskite solar cells. *Joule* *2*, 1961–1990.
- Meng, L., You, J., and Yang, Y. (2018). Addressing the stability issue of perovskite solar cells for commercial applications. *Nat. Commun.* *9*, 5265.
- Turren-Cruz, S.H., Hagfeldt, A., and Saliba, M. (2018). Methylammonium-free, high-performance, and stable perovskite solar cells on a planar architecture. *Science* *362*, 449–453.
- Kim, G., Min, H., Lee, K.S., Lee, D.Y., Yoon, S.M., and Seok, S.I. (2020). Impact of strain relaxation on performance of α -formamidinium lead iodide perovskite solar cells. *Science* *370*, 108–112.
- Li, N., Luo, Y., Chen, Z., Niu, X., Zhang, X., Lu, J., Kumar, R., Jiang, J., Liu, H., Guo, X., et al. (2020). Microscopic degradation in formamidinium-cesium lead iodide perovskite solar cells under operational stressors. *Joule* *4*, 1743–1758.
- Zhang, F., and Zhu, K. (2020). Additive engineering for efficient and stable perovskite solar cells. *Adv. Energy Mater.* *10*, 1902579.
- Yan, K., Long, M., Zhang, T., Wei, Z., Chen, H., Yang, S., and Xu, J. (2015). Hybrid halide perovskite solar cell precursors: colloidal chemistry and coordination engineering behind device processing for high efficiency. *J. Am. Chem. Soc.* *137*, 4460–4468.
- Zhang, Y., Liu, Y., Xu, Z., Ye, H., Yang, Z., You, J., Liu, M., He, Y., Kanatzidis, M.G., and Liu, S.F. (2020). Nucleation-controlled growth of superior lead-free perovskite Cs₃Bi₂I₉ single-crystals for high-performance X-ray detection. *Nat. Commun.* *11*, 2304.
- Li, Y., Wu, H., Qi, W., Zhou, X., Li, J., Cheng, J., Zhao, Y., Li, Y., and Zhang, X. (2020). Passivation of defects in perovskite solar cell: From a chemistry point of view. *Nano Energy* *77*, 105237.
- Mohd Yusoff, A.R.b., Vasilopoulou, M., Georgiadou, D.G., Palilis, L.C., Abate, A., and Nazeeruddin, M.K. (2021). Passivation and process engineering approaches of halide perovskite films for high efficiency and stability perovskite solar cells. *Energy Environ. Sci.* *14*, 2906–2953.
- Yang, W.S., Noh, J.H., Jeon, N.J., Kim, Y.C., Ryu, S., Seo, J., and Seok, S.I. (2015). SOLAR CELLS: High-performance photovoltaic perovskite layers fabricated through intramolecular exchange. *Science* *348*, 1234–1237.
- Lee, J.-W., Dai, Z., Lee, C., Lee, H.M., Han, T.-H., De Marco, N., Lin, O., Choi, C.S., Dunn, B., Koh, J., et al. (2018). Tuning molecular interactions for highly reproducible and efficient formamidinium perovskite solar cells via adduct approach. *J. Am. Chem. Soc.* *140*, 6317–6324.
- Bu, T., Li, J., Li, H., Tian, C., Su, J., Tong, G., Ono, L.K., Wang, C., Lin, Z., Chai, N., et al. (2021). Lead halide-templated crystallization of methylamine-free perovskite for efficient photovoltaic modules. *Science* *372*, 1327–1332.
- Hui, W., Chao, L., Lu, H., Xia, F., Wei, Q., Su, Z., Niu, T., Tao, L., Du, B., Li, D., et al. (2021). Stabilizing black-phase formamidinium perovskite formation at room temperature and high humidity. *Science* *371*, 1359–1364.
- Jeong, J., Kim, M., Seo, J., Lu, H., Ahlawat, P., Mishra, A., Yang, Y., Hope, M.A., Eickemeyer, F.T., Kim, M., et al. (2021). Pseudo-halide anion engineering for α -FAPbI₃ perovskite solar cells. *Nature* *592*, 381–385.
- Lu, H., Liu, Y., Ahlawat, P., Mishra, A., Tress, W.R., Eickemeyer, F.T., Yang, Y., Fu, F., Wang, Z., Avalos, C.E., et al. (2020). Vapor-assisted deposition of highly efficient, stable black-phase FAPbI₃ perovskite solar cells. *Science* *370*, eabb8985.
- Lee, J.-W., Kim, H.-S., and Park, N.-G. (2016). Lewis acid–base adduct approach for high efficiency perovskite solar cells. *Acc. Chem. Res.* *49*, 311–319.
- Luo, D., Li, X., Dumont, A., Yu, H., and Lu, Z.H. (2021). Recent progress on perovskite surfaces and interfaces in optoelectronic devices. *Adv. Mater.* *33*, e2006004.
- Xue, J., Wang, R., and Yang, Y. (2020). The surface of halide perovskites from Nano to bulk. *Nat. Rev. Mater.* *5*, 809–827.
- Jiang, Q., Zhao, Y., Zhang, X., Yang, X., Chen, Y., Chu, Z., Ye, Q., Li, X., Yin, Z., and You, J. (2019). Surface passivation of perovskite film for efficient solar cells. *Nat. Photonics* *13*, 460–466.
- Liu, Y., Akin, S., Hinderhofer, A., Eickemeyer, F.T., Zhu, H., Seo, J.-Y., Zhang, J., Schreiber, F., Zhang, H., Zakeeruddin, S.M., et al. (2020). Stabilization of highly efficient and stable phase-pure FAPbI₃ perovskite solar cells by molecularly tailored 2D-overlayers. *Angew. Chem. Int. Ed. Engl.* *59*, 15688–15694.
- Jeong, M., Choi, I.W., Go, E.M., Cho, Y., Kim, M., Lee, B., Jeong, S., Jo, Y., Choi, H.W., Lee, J., et al. (2020). Stable perovskite solar cells with efficiency exceeding 24.8% and 0.3-V voltage loss. *Science* *369*, 1615–1620.
- Li, Y., Li, Y., Shi, J., Zhang, H., Wu, J., Li, D., Luo, Y., Wu, H., and Meng, Q. (2018). High quality perovskite crystals for efficient film photodetectors induced by hydrolytic insulating oxide substrates. *Adv. Funct. Mater.* *28*, 1705220.
- Liu, Y., Sun, J., Yang, Z., Yang, D., Ren, X., Xu, H., Yang, Z., and Liu, S.F. (2016). 20-mm-large single-crystalline formamidinium-perovskite

- wafer for mass production of integrated photodetectors. *Adv. Opt. Mater.* **4**, 1829–1837.
30. Li, Y., Shi, J., Yu, B., Duan, B., Wu, J., Li, H., Li, D., Luo, Y., Wu, H., and Meng, Q. (2020). Exploiting electrical transients to quantify charge loss in solar cells. *Joule* **4**, 472–489.
31. Wu, J., Shi, J., Li, Y., Li, H., Wu, H., Luo, Y., Li, D., and Meng, Q. (2019). Quantifying the interface defect for the stability origin of perovskite solar cells. *Adv. Energy Mater.* **9**, 1901352.
32. Tan, S., Shi, J., Yu, B., Zhao, W., Li, Y., Li, Y., Wu, H., Luo, Y., Li, D., and Meng, Q. (2021). Inorganic ammonium halide additive strategy for highly efficient and stable CsPbI₃ perovskite solar cells. *Adv. Funct. Mater.* **31**, 2010813.
33. Zhumekenov, A.A., Burlakov, V.M., Saidaminov, M.I., Alofi, A., Haque, M.A., Turedi, B., Davaasuren, B., Dursun, I., Cho, N., El-Zohry, A.M., et al. (2017). The role of surface tension in the crystallization of metal halide perovskites. *ACS Energy Lett* **2**, 1782–1788.
34. Li, H., Shi, J., Deng, J., Chen, Z., Li, Y., Zhao, W., Wu, J., Wu, H., Luo, Y., Li, D., and Meng, Q. (2020). Intermolecular π - π Conjugation Self-Assembly to Stabilize Surface Passivation of Highly Efficient perovskite Solar Cells. *Adv. Mater.* **32**, e1907396.
35. Yang, X., Luo, D., Xiang, Y., Zhao, L., Anaya, M., Shen, Y., Wu, J., Yang, W., Chiang, Y.-H., Tu, Y., et al. (2021). Buried interfaces in halide perovskite photovoltaics. *Adv. Mater.* **33**, e2006435.
36. Rolston, N., Scheideler, W.J., Flick, A.C., Chen, J.P., Elmaraghi, H., Sleugh, A., Zhao, O., Woodhouse, M., and Dauskardt, R.H. (2020). Rapid open-air fabrication of perovskite solar modules. *Joule* **4**, 2675–2692.

Joule, Volume 6

Supplemental information

**Efficient, stable formamidinium-cesium
perovskite solar cells and minimodules
enabled by crystallization regulation**

**Yiming Li, Zijing Chen, Bingcheng Yu, Shan Tan, Yuqi Cui, Huijue Wu, Yanhong
Luo, Jiangjian Shi, Dongmei Li, and Qingbo Meng**

Supplemental items

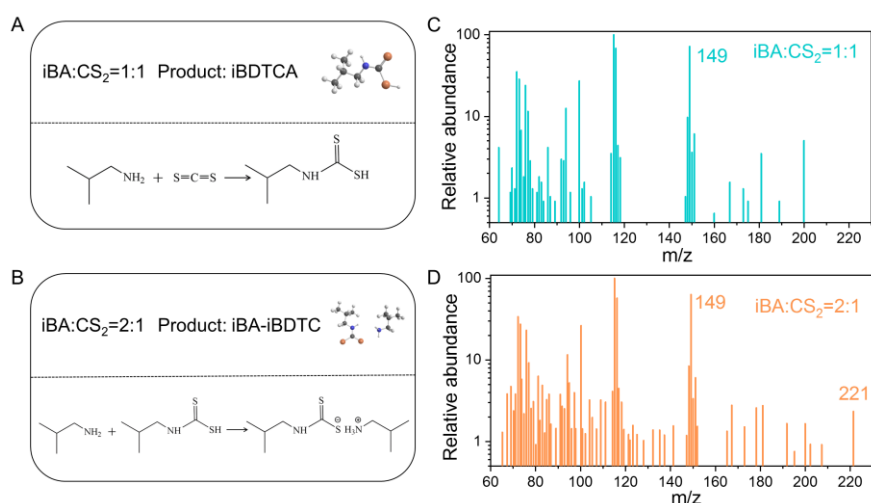


Figure S1. The schematic diagram for the reaction of iBA with CS₂ at a molar ratio of 1:1 (A) and 2:1 (B), respectively. Corresponding mass spectra of reaction products for the reaction of iBA with CS₂ at a molar ratio of 1:1 (C) and 2:1 (D).

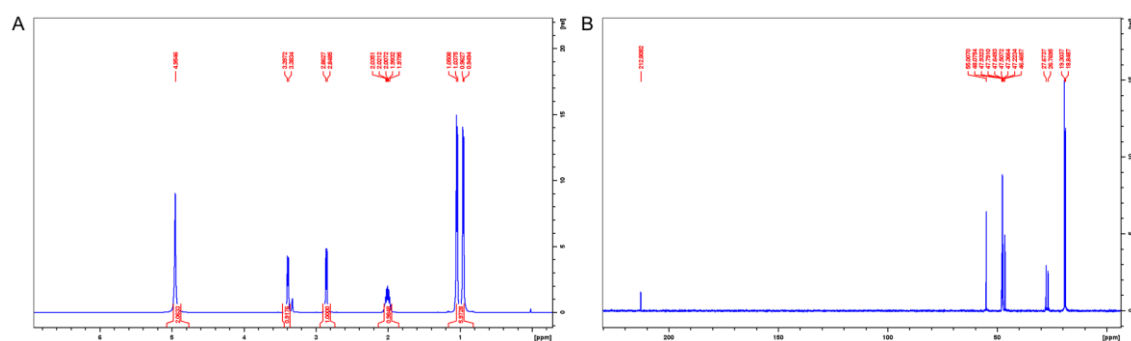


Figure S2. ¹H NMR data (A) and ¹³C NMR data (B) of iBA-iBDTC material.

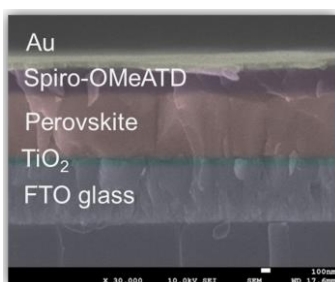


Figure S3. A representative cross-sectional SEM image of iBA-iBDTC modified PSCs. The thickness of the perovskite film is 716.67 nm.

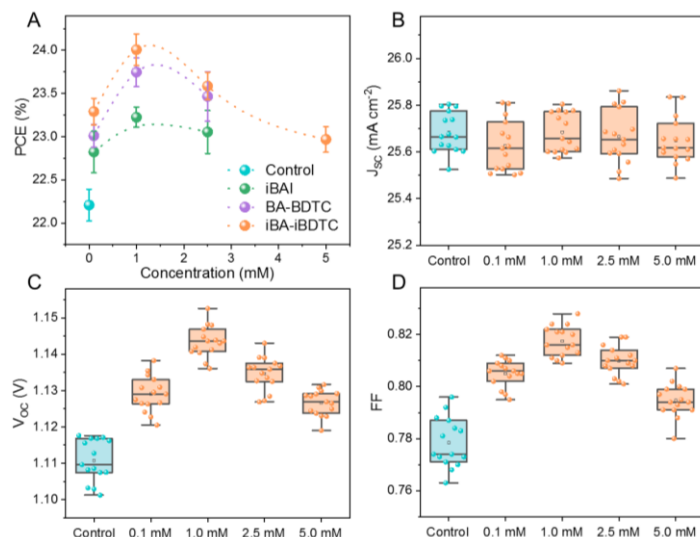


Figure S4. Device performance statistics with different modifications in antisolvent under the optimization of concentration. (A) PCE distribution of PSCs. Detailed J_{sc} (B), V_{oc} (C) and FF (D) statistics of PSCs with iBA-iBDTC modification under the optimization of concentration.

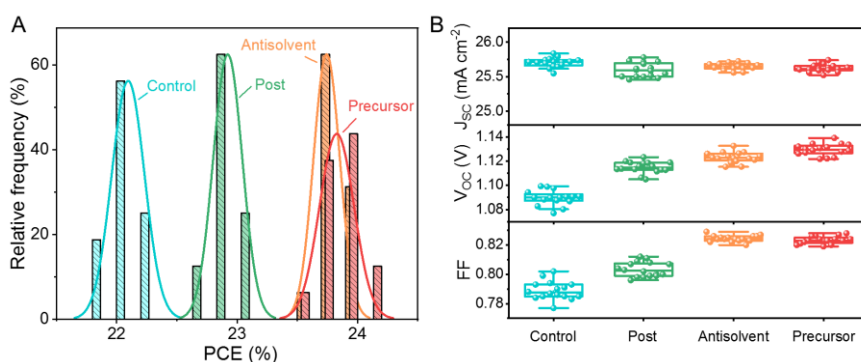


Figure S5. Device performance statistics with iBA-iBDTC modification introduced in different ways. (A) PCE distribution histograms. (B) Detailed performance parameters statistics.

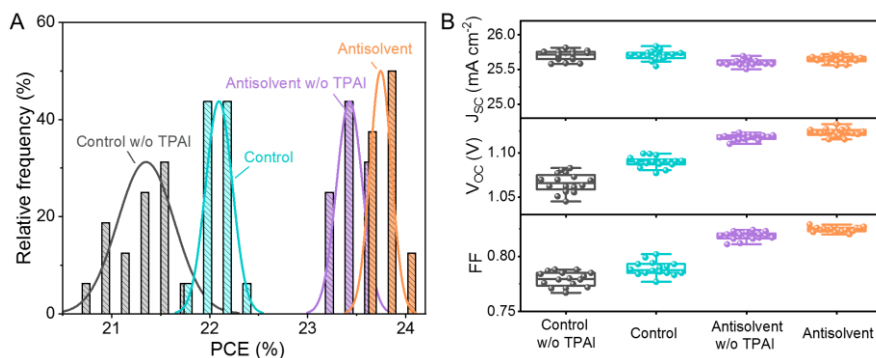


Figure S6. Device performance statistics with and without TPAI post-treatment process. (A) PCE distribution histograms. (B) Detailed performance parameters statistics.

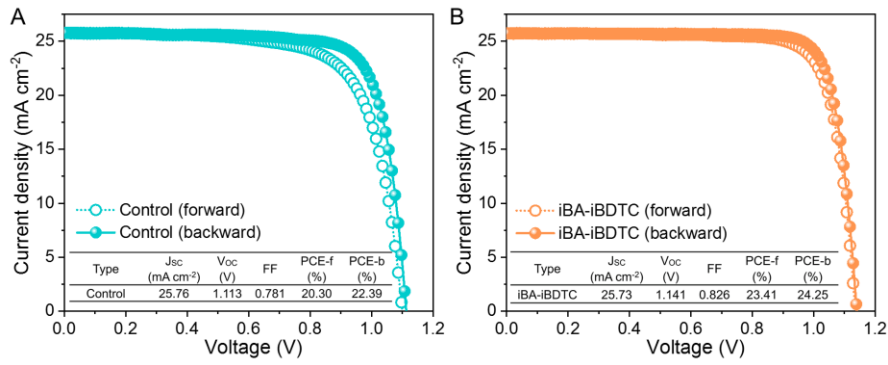


Figure S7. Current-voltage characteristic curves (including forward and backward scan) of the typical cells without (A) or with (B) the iBA-iBDTC modification.

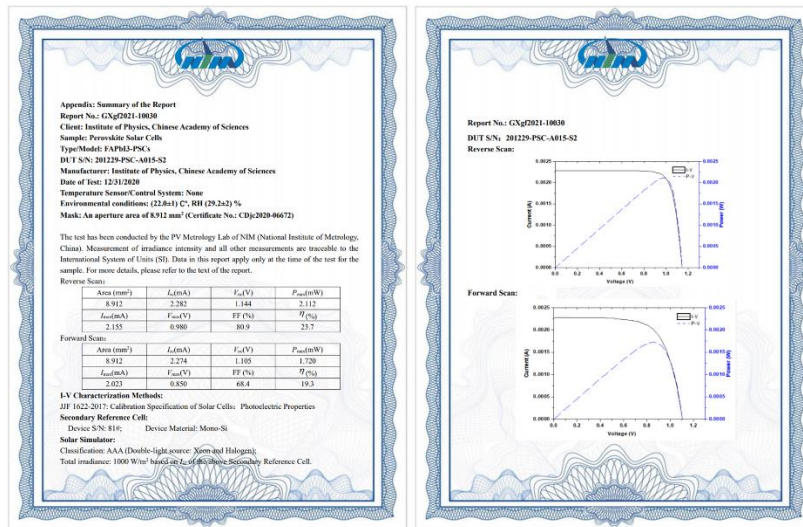


Figure S8. Certificated results by the National Institute of Metrology, China (NIM, China).

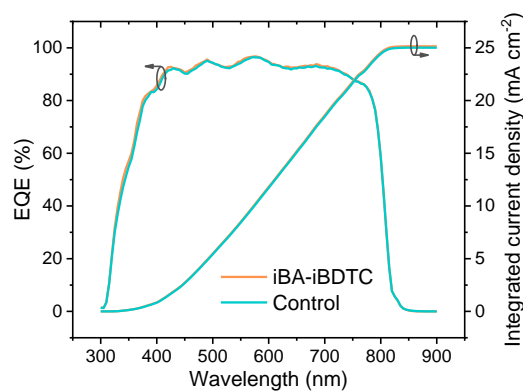


Figure S9. Typical external quantum efficiency (EQE) and integrated current density spectra of the control and modified devices.

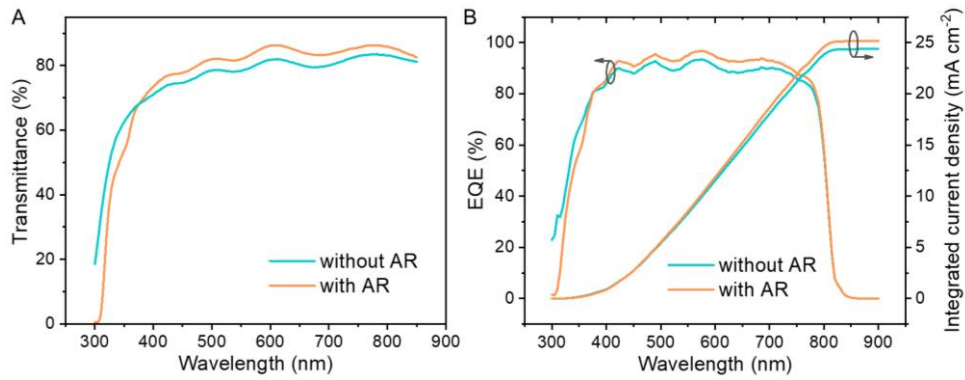


Figure S10. Characterization of antireflection coating. (A) Transmittance spectra of FTO glasses with and without antireflection coating (AR). (B) EQE and integrated current density spectra of typical device with and without AR (~3% enhancement in current density).

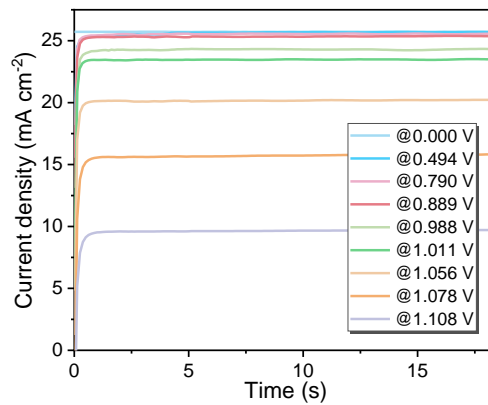


Figure S11. Steady-state current density outputs of the champion modified cell at different voltage bias during the quasi-steady-state (QSS) measurement.

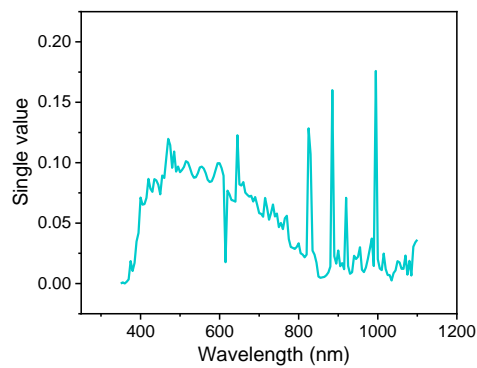


Figure S12. Calibration spectra of solar simulator used for measurement at November 18th, 2019 with no additional filters.

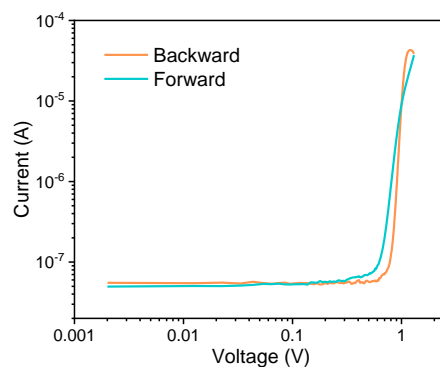


Figure S13. Typical dark current-voltage characteristics in both sweep directions.

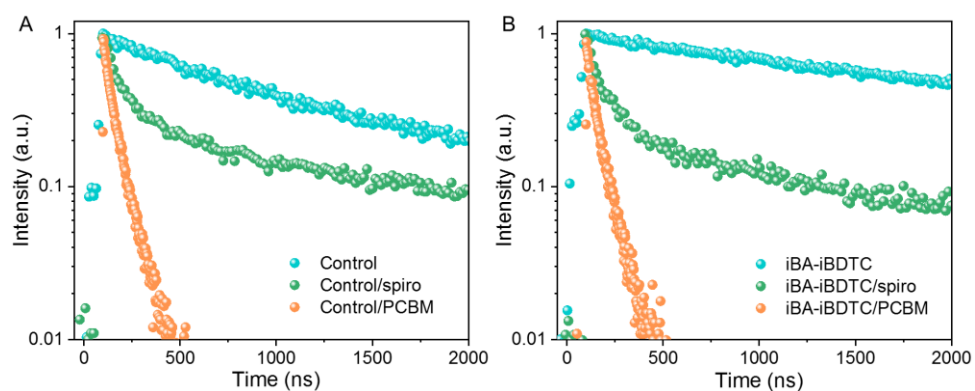


Figure S14. TRPL decay curves for perovskite films without (A) and with (B) iBA-iBDTC modification covered with different carrier extraction films.

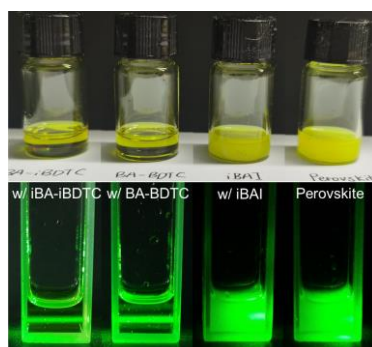


Figure S15. Photographs of perovskite precursor solutions in N,N-Dimethylformamide with different additives and their Tyndall effect.

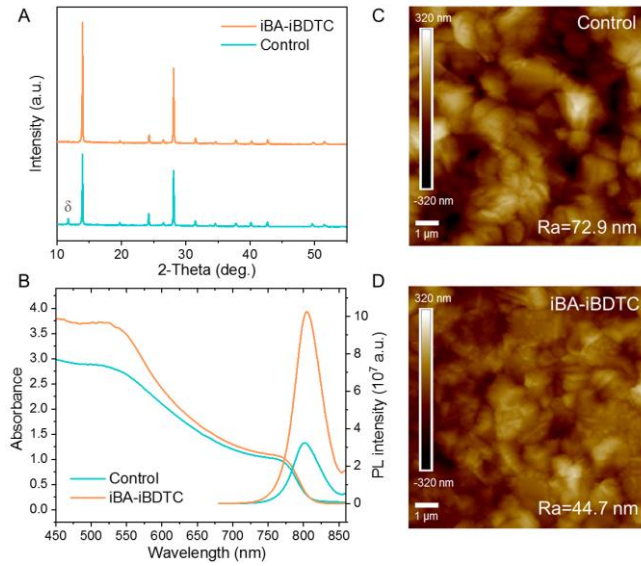


Figure S16. XRD and AFM characterization of perovskite films with and without iBA-iBDTC modification. (A) XRD patterns of layered perovskite films. (B) Corresponding steady-state PL and visible-light absorption spectra of different films. AFM images of perovskite films without (C) and with (D) iBA-iBDTC modification.

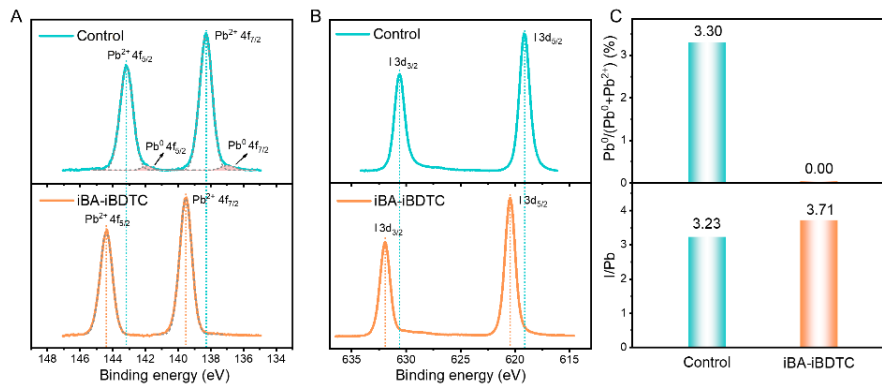


Figure S17. X-ray photoelectron spectroscopy (XPS) results of Pb 4f (A), and I 3d (B) for perovskite films. (C) Fitting results of the Pb⁰/(Pb⁰+Pb²⁺) ratio (up), and fitting results of I/Pb ratio (down).

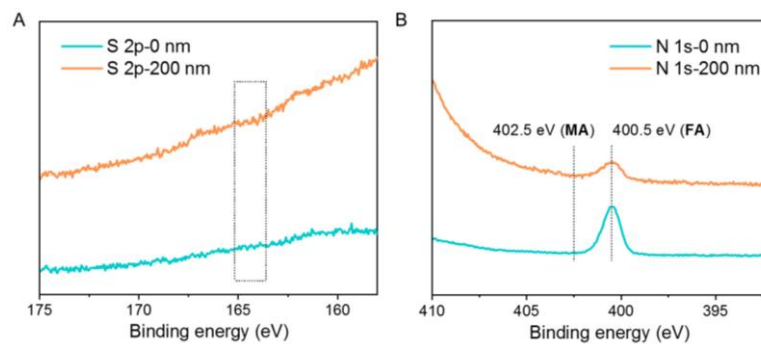


Figure S18. X-ray photoelectron spectroscopy (XPS) results of S 2p (A) and N 1s (B) for iBA-iBDTC modified perovskite sample at 0 nm and 200 nm depth using Ar⁺ ion sputtering sources.

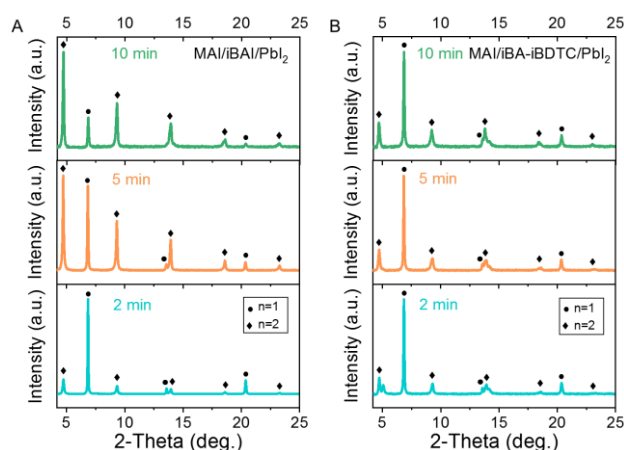


Figure S19. XRD characterization of MAI and PbI_2 films modified by different materials. (A) XRD patterns of MAI and PbI_2 films modified by iBAI at 150 °C annealing temperature with different annealing time. (B) XRD patterns of MAI and PbI_2 films modified by iBA-iBDTC at 150 °C annealing temperature with different annealing time.

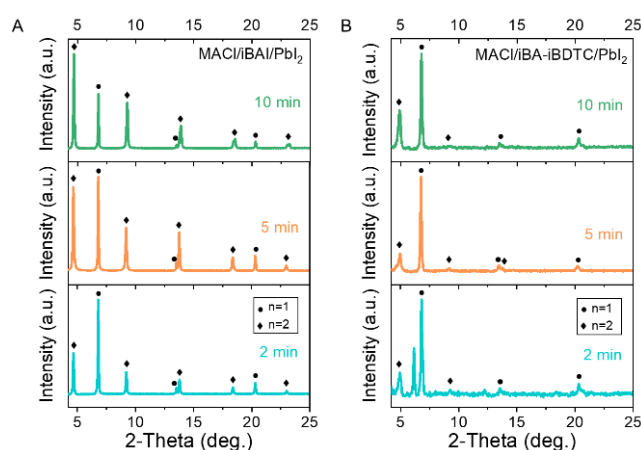


Figure S20. XRD characterization of MACl and PbI_2 films modified by different materials. (A) XRD patterns of MACl and PbI_2 films modified by iBAI at 150 °C annealing temperature with different annealing time. (B) XRD patterns of MACl and PbI_2 films modified by iBA-iBDTC at 150 °C annealing temperature with different annealing time.

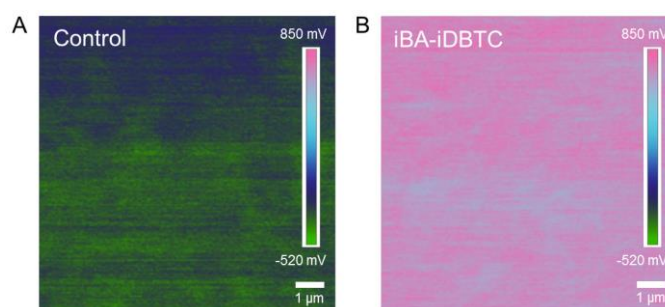


Figure S21. KPFM surface potential distribution of perovskite films without (A) and with (B) iBA-iBDTC modification.

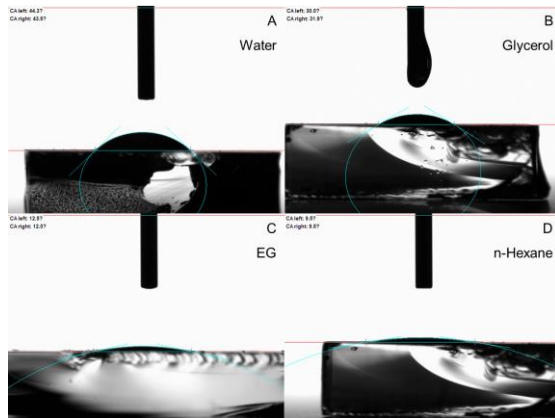


Figure S22. Contact angles of the control perovskite film with (A) water, (B) glycerol, (C) EG, and (D) n-hexane solution droplets, respectively.

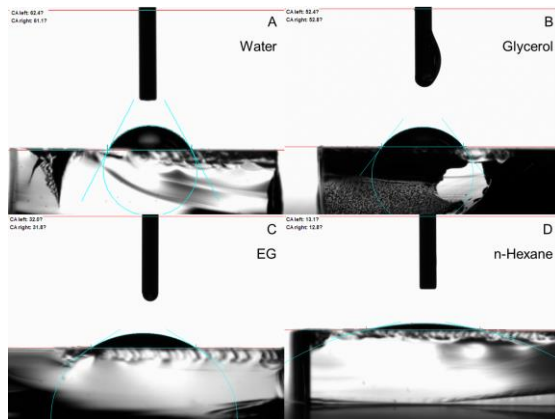


Figure S23. Contact angles of the iBA-iBDTC modified perovskite film with (A) water, (B) glycerol, (C) EG, and (D) n-hexane solution droplets, respectively.

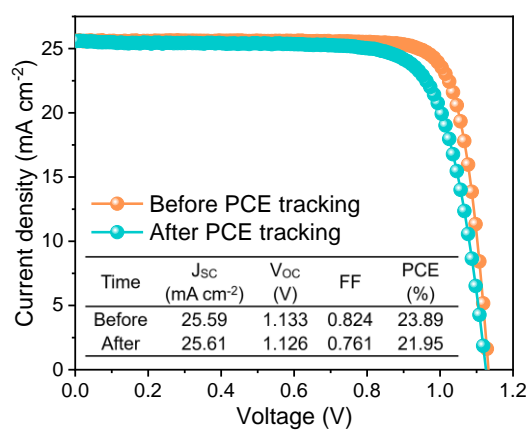


Figure S24. J - V curves of the iBA-iBDTC modified device before and after 500 h operational stability tracking.

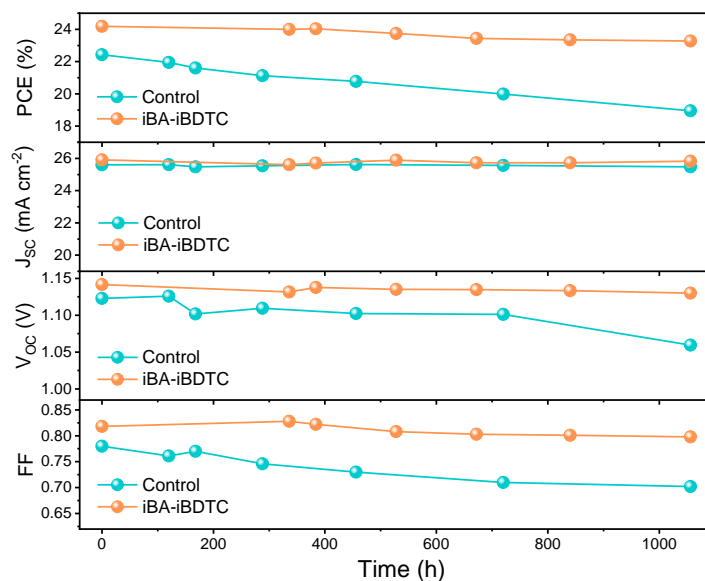


Figure S25. PCE, J_{sc} , V_{oc} and FF tracking of non-encapsulated cells stored in ambient conditions (temperature: 25 °C, relative humidity: 20~30%) for 1000 h.

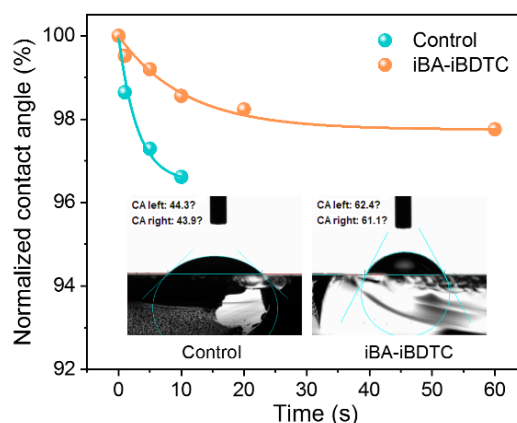


Figure S26. Time-dependent water contact angle measurements for different perovskite films, insets are water contact angles of perovskite films at 0 s.

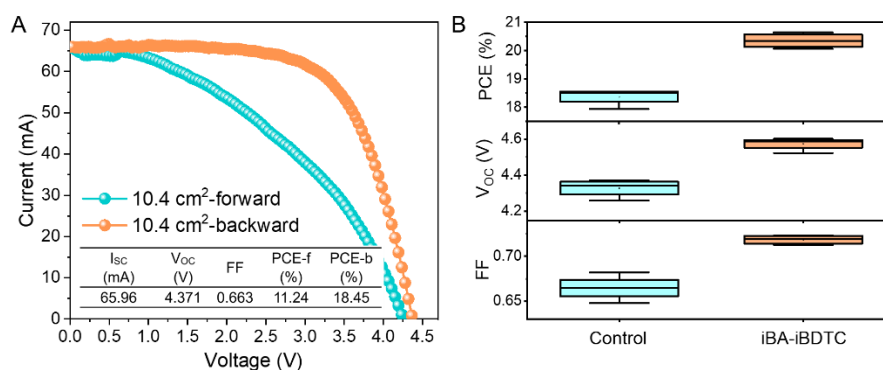


Figure S27. Minimodule performance statistics with and without modification. (A) Typical I - V curve of the control minimodule device (an active area of 10.4 cm²). (B) Detailed performance parameters statistics of minimodule devices with and without iBA-iBDTC modification.

Table S1. Statistical performance of FA-based control devices benchmarked to literature.

Structure	J_{sc} (mA cm ⁻²)	V_{oc} (V)	FF	PCE (%)	Reference
FTO/c-TiO ₂ /(FA _{0.97} CS _{0.03})Pb(I _{0.97} Br _{0.03}) ₃ / spiro-OMeTAD/Au	25.68	1.104	0.797	22.60	This work
FTO/c-TiO ₂ /m-TiO ₂ /FAPbI ₃ / spiro-OMeTAD/Au	25.72	1.153	0.807	23.92	[1]
FTO/c-TiO ₂ /m-TiO ₂ /FAPbI ₃ / spiro-OMeTAD/Au	26.04	1.152	0.781	23.44	[2]
ITO/SnO ₂ /FAPbI ₃ / spiro-OMeTAD/MoO ₃ /Au	24.72	1.150	0.778	22.14	[3]
FTO/SnO ₂ /FAPbI ₃ / spiro-OMeTAD/Ag	24.15	1.114	0.808	21.72	[4]
FTO/c-TiO ₂ /m-TiO ₂ /FAPbI ₃ / spiro-OMeTAD/Au	25.87	1.053	0.772	21.03	[5]
FTO/SnO ₂ /FA _{0.83} CS _{0.17} PbI ₃ / spiro-OMeTAD/Au	24.01	1.142	0.755	20.71	[6]
ITO/SnO ₂ /(FA _{0.9} CS _{0.1})PbI ₃ / spiro-OMeTAD/Au	23.72	1.092	0.781	20.23	[7]
ITO/SnO ₂ /FA _{0.98} CS _{0.02} PbI ₃ / spiro-OMeTAD/Ag	23.98	1.095	0.769	20.19	[8]
FTO/SnO ₂ /(FA _{0.9} CS _{0.1})PbI ₃ / spiro-OMeTAD/Au	24.55	1.088	0.720	19.23	[9]
ITO/SnO ₂ /FAPbI ₃ / spiro-OMeTAD/Au	23.12	1.098	0.707	17.95	[10]

Table S2. Statistical J_{sc} of champion target FA-based devices benchmarked to literature.

Structure	J_{sc} (mA cm ⁻²)	E_g (eV)	Reference
FTO/c-TiO ₂ / (FA _{0.97} CS _{0.03})Pb(I _{0.97} Br _{0.03}) ₃ / spiro-OMeTAD/Au	25.76	1.50	This work
FTO/c-TiO ₂ /m-TiO ₂ /FAPbI ₃ / spiro-OMeTAD/Au	26.35	1.49	[1]
FTO/c-TiO ₂ /m-TiO ₂ /FAPbI ₃ / spiro-OMeTAD/Au	26.35	1.50	[2]
FTO/c-TiO ₂ /m-TiO ₂ / (FAPbI ₃) _{0.97} (MDA,Cs) _{0.03} / spiro-OMeTAD/Au	26.23	1.51	[11]
FTO/c-TiO ₂ /m-TiO ₂ /FAPbI ₃ / spiro-OMeTAD/Au	25.87	1.48	[5]
ITO/SnO ₂ /(FA _{0.95} MA _{0.035} CS _{0.015})PbI ₃ / SEB/Au	26.14	1.52	[12]

ITO/SnO ₂ /FAPbI ₃ / spiro-OMeTAD/MoO ₃ /Au	25.62	1.53	[3]
---	-------	------	-----

Table S3. Contact angles between the liquids with known polar and dispersive components of surface tension and the perovskite films without or with iBA-iBDTC modification.

Solvent(L)	Surface Tension (mN/m)			Contact angle $\theta(^{\circ})$	x	y	k	y ₀
	Total σ^{tot}	Disperse σ^{d}	Polar σ^{p}					
(A) Control perovskite film								
Water	72.30	18.70	53.60	44.3	1.69	14.34	6.03	4.16
Glycerol	63.30	20.22	43.08	30.0	1.46	13.13		
EG	48.00	29.00	19.00	12.5	0.81	8.81		
n-Hexane	18.43	18.43	0.00	9.5	0.00	4.26		
(B) iBA-iBDTC modified perovskite film								
Water	72.30	18.70	53.60	62.4	1.69	12.23	4.76	4.30
Glycerol	63.30	20.22	43.08	52.4	1.46	11.33		
EG	48.00	29.00	19.00	32.0	0.81	8.24		
n-Hexane	18.43	18.43	0.00	13.1	0.00	4.24		

Supplemental Experimental Procedures

Note S1. Characterization of synthesized isobutylammonium dithiocarbamate salt

The dual-functional isobutylammonium dithiocarbamate salt iBA-iBDTC is synthesized by the reaction of organic isobutylamine (iBA) with carbon disulfide (CS₂) at a molar ratio of 2:1. For comparison, the intermediate product isobutyldithiocarbamic acid iBDTCA (1:1 molar ratio) is also provided. The products were characterized by mass spectra (HRMS-MALDI-TOF) presented in Figure S1(C-D). ¹H, ¹³C nuclear magnetic resonance spectroscopy (NMR) of iBA-iBDTC material are performed in Figure S2(A-B). Detailed analytic results are given in Experimental Procedures part.

Note S2. Characterization of device structure and device performance

We introduce the iBA-iBDTC additive in the perovskite precursor solution (denoted as Precursor), antisolvent (denoted as Antisolvent), and post-treatment process (denoted as Post), respectively. Corresponding perovskite solar cells are fabricated. The PCE statistic histograms of these cells are presented in Figure S5(A). The Precursor devices exhibit similar performance to the Antisolvent devices. This result confirms that the CSS⁻ plays similar roles in regulating the nucleation and crystallization process for the perovskite system. The Post devices perform with an obvious lower average PCE of 22.92%. When only using a post process, the additive can hardly fully interact with the perovskite and thus cannot play the maximum regulation effect. The detailed statistical distributions of short-circuit current density (J_{sc}), open-circuit voltage (V_{oc}), and fill factor (FF) of the cells are given in Figure S5(B) (Supplemental Information). Compared to control devices, the devices with iBA-iBDTC modifications introduced in different ways all exhibit improvement in V_{oc} and FF. The iBA-iBDTC can be introduced into perovskite

precursor solution to make compatible with the scaling up method.

Note S3. Time-resolved photoluminescence (TRPL) measurements and the calculation of carrier diffusion coefficient in different perovskite films

To estimate carrier diffusion coefficient, the TRPL decay curves of different perovskite films covered without and with hole extraction (spiro-OMeTAD) or electron extraction (PCBM) layers were measured, as presented in Figure S14. In this case, we can use a simple diffusion limited extraction model in a bilayer system to estimate carrier diffusion lengths.¹³

According to the literature, charge carrier diffusion lengths can be calculated, using the formula,¹⁴⁻¹⁵

$$\frac{\tau_0}{\tau_{ex}} = 1 + \frac{\pi^2}{4} \times \left(\frac{L_D}{L}\right)^2 \quad (1)$$

where τ_0 and τ_{ex} are lifetimes of TRPL measurements for perovskite films without and with carrier extraction layers, respectively, L_D is the carrier diffusion length of perovskites and L is the thickness of perovskite layer. By assuming that carrier extraction occurs only at the extraction layer interface with 100% efficiency, using the corresponding experimental scatters for extraction ratios, the minimum estimates of carrier diffusion lengths can be obtained.

Note S4. Calculation of interface defects

An expanded equivalent circuit model and corresponding admittance spectroscopy analysis is introduced. The model is simplified from a much more complicated strategy that was initially utilized for a metal-insulator-semiconductor structure.¹⁶ As presented in Figure 2(F), besides a widely used paralleled element consisting of charge transfer resistance (R_{sh}) and bulk junction capacitance (C_d), the expanded equivalent circuit model contains another capacitance (C_{ss}) to reflect the interface defect response. The R_{ss} is the resistance that a charge needs before being captured by the interface defect.¹⁷ There is a quantitative relationship between C_{ss} and the interface defect density (N_{ss}), that is,¹⁸

$$C_{ss} = qAN_{ss}, \quad (2)$$

where q is the electron charge and A is the device area. With this theoretical model, the experimental admittance measurements can be fitted using the formula,¹⁶

$$\frac{1}{\omega} \left(G - \frac{1}{R_{sh}} \right) = \frac{\omega R_{ss} C_{ss}^2}{1 + (\omega R_{ss} C_{ss})^2}, \quad (3)$$

where G is the admittance and ω is the angular frequency. In this case, the C_{ss} as well as the N_{ss} can then be computed from the admittance spectra.

Note S5. Material and chemistry mechanism characterization

Figure S16(A) presents XRD patterns of perovskite films with and without iBA-iBDTC modification, and from higher diffraction peak intensity, better crystallinity of iBA-iBDTC sample is further confirmed. Besides, our results demonstrate that the control film contains photo-inactive yellow δ -phase $FAPbI_3$ with obvious diffraction peak at 11.8° . However, for iBA-iBDTC modified sample, δ -phase is effectively suppressed, together with the overall signal enhancement, indicating the better crystalline and phase stabilization ability of CSS-Pb coordination effect. The steady-state PL and visible-light absorption spectra were further explored to study the influence of passivation, as shown in Figure S16(B). Both PL peak

positions behave fairly close to their absorption edges, implying perovskite band-tail states have been suppressed. It is obvious that iBA-iBDTC sample exhibits much better radiative capacity with ~3.2 PL enhancement, implying much lower trap density. Besides, we imaged the surface morphology of iBA-iBDTC and control samples using atomic force microscopy (AFM). As presented in Figure S16(C-D), smaller surface roughness ($R_a \sim 44.7$ nm) of iBA-iBDTC sample can be obtained.

For the control sample (Figure S17(A)), the binding energy (BE) at 143.2 and 138.3 eV are assigned to $4f_{5/2}$ and $4f_{7/2}$ of divalent Pb^{2+} , respectively. The two corresponding shoulder peaks at 141.9 and 136.9 eV around lower BE are associated with metallic Pb^0 , which is a primary deep defect state that severely degrades the performance of perovskite optoelectronic devices, as well as their long-term durability.¹⁹⁻²⁰ The intensity ratio of $Pb^0/(Pb^0+Pb^{2+})$ for the control sample is further calculated in Figure S17(C), the Pb^0 intensity ratio reaches ~3.3%. As for iBA-iBDTC modified sample, single peaks assigned to $4f_{5/2}$ and $4f_{7/2}$ of divalent Pb^{2+} without any lower energy shoulder can be observed, indicating the production of metallic Pb^0 has been successfully eliminated. This should be attributed to interaction between CSS^- anion and Pb^{2+} during the nucleation and crystal growth of the perovskite films, resulting in better crystalline perovskite films with Pb^0 deep defects effectively suppressed. With respect to I^0 species, it is difficult to obtain $I^0/(I^0+I^-)$ ratio by peak fitting because I^0 species are volatile during the annealing process of perovskite film preparation. Thus, as literature reported,¹⁹ the ratio of I/Pb is applied to monitor the iodine evolution indirectly. As presented in Figure S17(C), a higher I/Pb ratio can be observed in iBA-iBDTC modified sample, indicating less volatile I^0 species produced in the corresponding film. And potential interaction via ionic bonding between iBA^+ cations and under-coordinated I^- ions should be the reason for the suppression of I^0 deep defects.

It should be noted that pure iBA-iBDTC material can only withstand 90 °C annealing temperature (Figure 3(F)). When the temperature reaches up to 150 °C, only PbI_2 peak at 12.7° retains in iBA-iBDTC/ PbI_2 sample (Figure 3(G)). In this case, extra methylammonium iodide (MAI, 1M) was added in these precursor solutions above. Corresponding films and XRD patterns are performed. At 150 °C, both MAI/iBA-iBDTC/ PbI_2 and MAI/iBAI/ PbI_2 samples exhibit layered quasi-2D perovskite phase $(iBA)_2(MA)_{n-1}Pb_nI_{3n+1}$ ($n=1$ and $n=2$) in Figure 3(G). With the participation of MAI, quasi-2D phase in MAI/iBAI/ PbI_2 sample tends to convert from $n=1$ to $n=2$ phase as the annealing time increases (Figure S19(A)), and when the annealing time reaches 10 min, $n=2$ phase dominates. However, for MAI/iBA-iBDTC/ PbI_2 sample, this phase transition process is no longer obvious, even when the annealing time reaches 10 min, $n=1$ phase still dominates, indicating a disappearance process of MA^+ occurs (Figure S19(B)). Similar phenomenon also appears when introducing MAI to iBAI/ PbI_2 and iBA-iBDTC/ PbI_2 systems (Figure S20(A-B)). Combined with XPS results, it can be speculated that iBDTC⁻ anion only participates in perovskite crystalline process and then synergistically volatilizes by forming volatile CH_3NH_2 and $(CH_3)_2CHCH_2NH_2$; while retained iBA^+ cation will incorporate into the interval of surface Pb-I octahedrons and uniformly distribute on the film surface and grain boundaries for realizing passivation effect.

Note S6. The surface energy characterization for different films

The surface energy of perovskite films can be estimated using Owens-Wendt-Rabel-Kaelble (OWRK) method.²¹ Based on the formula,

$$\frac{\sigma_L(\cos\theta+1)}{2\sqrt{\sigma_L^d}} = \sqrt{\sigma_S^p} \sqrt{\frac{\sigma_L^p}{\sigma_L^d}} + \sqrt{\sigma_S^d}, \quad (4)$$

where θ represents for the contact angle, σ_S -surface energy of a solid, σ_L -surface tension of a liquid, d and p refer to dispersive and polar components of surface energy, respectively. If we let,

$$x = \sqrt{\sigma_L^p}/\sqrt{\sigma_L^d}, y = \sigma_L(\cos\theta + 1)/(2\sqrt{\sigma_L^d}), k = \sqrt{\sigma_S^p}, y_0 = \sqrt{\sigma_S^d},$$

then, a simple linear function, $y = kx + y_0$ can be obtained. From the slope and intercept of the plotted line, the polar and dispersive components of solid's surface energy, respectively, can be calculated.

Note S7. Detailed characterization for device stability test

To test water resistance performance, time-dependent water contact angle measurements were conducted, as show in Figure S26. In the initial stage, iBA-iBDTC modified perovskite film exhibits much higher water contact angle of over 60° , which demonstrates that the iBA⁺ cation coating blanket on perovskite surface exhibits certain hydrophobicity. After directly contacting with water droplet for 60 s, the contact angle decreases to a primarily stable value of over 58° , and still behaves well water resistance performance, confirming that the formation of this coating blanket can realize a significantly improved moisture stability of perovskite films.

Supplemental References

1. Jeong, J., Kim, M., Seo, J., Lu, H., Ahlawat, P., Mishra, A., Yang, Y., Hope, M.A., Eickemeyer, F.T., Kim, M., Yoon, Y.J., Choi, I.W., Darwich, B.P., Choi, S.J., Jo, Y., Lee, J.H., Walker, B., Zakeeruddin, S.M., Emsley, L., Rothlisberger, U., Hagfeldt, A., Kim, D.S., Grätzel, M., and Kim, J.Y. (2021). Pseudo-halide anion engineering for α -FAPbI₃ perovskite solar cells. *Nature* 592, 381–385.
2. Jeong, M., Choi, I.W., Go, E.M., Cho, Y., Kim, M., Lee, B., Jeong, S., Jo, Y., Choi, H.W., Lee, J., Bae, J.H., Kwak, S.K., Kim, D.S., and Yang, C. (2020). Stable perovskite solar cells with efficiency exceeding 24.8% and 0.3-V voltage loss. *Science* 369, 1615–1620.
3. Hui, W., Chao, L., Lu, H., Xia, F., Wei, Q., Su, Z., Niu, T., Tao, L., Du, B., Li, D., Wang, Y., Dong, H., Zuo, S., Li, B., Shi, W., Ran, X., Li, P., Zhang, H., Wu, Z., Ran, C., Song, L., Xing, G., Gao, X., Zhang, J., Xia, Y., Chen, Y., and Huang, W. (2021). Stabilizing black-phase formamidinium perovskite formation at room temperature and high humidity. *Science* 371, 1359–1364.
4. Zhang, Y., Seo, S., Lim, S.Y., Kim, Y., Kim, S.G., Lee, D.K., Lee, S.H., Shin, H., Cheong, H., and Park N.G. (2020). Achieving Reproducible and High-Efficiency (>21%) Perovskite Solar Cells with a Presynthesized FAPbI₃ Powder. *ACS Energy Lett.* 5, 360–366.
5. Liu, Y., Akin, S., Hinderhofer, A., Eickemeyer, F.T., Zhu, H., Seo, J.Y., Zhang, J., Schreiber, F., Zhang, H., Zakeeruddin, S.M., Hagfeldt, A., Dar, M.I., and Grätzel, M. (2020). Stabilization of Highly Efficient and Stable Phase-Pure FAPbI₃ Perovskite Solar Cells by Molecularly Tailored 2D-Overlayers. *Angew. Chem. Int. Ed.* 59, 15688–15694.
6. Bu, T., Li, J., Li, H., Tian, C., Su, J., Tong, G., Ono, L.K., Wang, C., Lin, Z., Chai, N., Zhang, X.L., Chang, J., Lu, J., Zhong, J., Huang, W., Qi, Y., Cheng, Y.B., and Huang, F. (2021).

Lead halide-templated crystallization of methylamine-free perovskite for efficient photovoltaic modules. *Science* 372, 1327–1332.

7. Li, N., Luo, Y., Chen, Z., Niu, X., Zhang, X., Lu, J., Kumar, R., Jiang, J., Liu, H., Guo, X., Lai, B., Brocks, G., Chen, Q., Tao, S., Fenning, D.P., and Zhou, H. (2020). Microscopic Degradation in Formamidinium-Cesium Lead Iodide Perovskite Solar Cells under Operational Stressors. *Joule* 4, 1–16.
8. Lee, J.W., Dai, Z., Lee, C., Lee, H.M., Han, T.H., De Marco, N., Lin, O., Choi, C.S., Dunn, B., Koh, J., Carlo, D.D., Ko, J.H., Maynard, H.D., and Yang, Y. (2018). Tuning Molecular Interactions for Highly Reproducible and Efficient Formamidinium Perovskite Solar Cells via Adduct Approach. *J. Am. Chem. Soc.* 140, 6317–6324.
9. Turren-Cruz, S.H., Hagfeldt, A., and Saliba, M. (2018). Methylammonium-free, high-performance, and stable perovskite solar cells on a planar architecture. *Science* 362, 449–453.
10. Lu, H., Liu, Y., Ahlawat, P., Mishra, A., Tress, W.R., Eickemeyer, F.T., Yang, Y., Fu, F., Wang, Z., Avalos, C.E., Carlsen, B.I., Agarwalla, A., Zhang, X., Li, X., Zhan, Y., Zakeeruddin, S.M., Emsley, L., Rothlisberger, U., Zheng, L., Hagfeldt, A., and Grätzel, M. (2020). Vapor-assisted deposition of highly efficient, stable black-phase FAPbI₃ perovskite solar cells. *Science* 370, eabb8985.
11. Kim, G., Min, H., Lee, K.S., Lee, D.Y., Yoon, S.M., and Seok, S.I. (2020). Impact of strain relaxation on performance of α -formamidinium lead iodide perovskite solar cells. *Science* 370, 108–112.
12. Zai, H., Su, J., Zhu, C., Chen, Y., Ma, Y., Zhang, P., Ma, S., Zhang, X., Xie, H., Fan, R., Huang, Z., Li, N., Zhang, Y., Li, Y., Bai, Y., Gao, Z., Wang, X., Hong, J., Sun, K., Chang, J., Zhou, H., and Chen, Q. (2021). Sandwiched electrode buffer for efficient and stable perovskite solar cells with dual back surface fields. *Joule* 5, 2148–2163.
13. Xing, G., Mathews, N., Sun, S., Lim, S., Lam, Y. M., Grätzel, M., Mhaisalkar, S., and Sum, T. C. (2013). Long-Range Balanced Electron- and Hole-Transport Lengths in Organic-Inorganic CH₃NH₃PbI₃. *Science* 342, 344–347.
14. Sproul, A. B. (1994). Dimensionless solution of the equation describing the effect of surface recombination on carrier decay in semiconductors. *J. Appl. Phys.* 76, 2851-2854.
15. Lim, S. S., Chong, W. K., Solanki, A., Dewi, H. A., Mhaisalkar, S., Mathews, N., and Sum, T. C. (2016). Modulating carrier dynamics through perovskite film engineering. *Phys. Chem. Chem. Phys.* 18, 27119-27123.
16. Brus, V. V. (2012). On impedance spectroscopy analysis of nonideal heterojunctions. *Sci. Technol.* 27, 035024.
17. Lehovc, K., and Slobodskoy, A. (1964). Impedance of semiconductor-insulator-metal capacitors. *Solid-State Electron.* 7, 59-79.
18. Sze, S. M., and Ng, K. K. (2007). *Physics of Semiconductor Devices* (3rd Edition), (John Wiley & Sons, Hoboken, New Jersey).
19. Wang, L., Zhou, H., Hu, J., Huang, B., Sun, M., Dong, B., Zheng, G., Huang, Y., Chen, Y., Li, L., Xu, Z., Li, N., Liu, Z., Chen, Q., Sun, L.D., and Yan, C.H. (2019). A Eu³⁺-Eu²⁺ ion redox shuttle imparts operational durability to Pb-I perovskite solar cells. *Science* 363, 265–270.

20. Dou, J., Zhu, C., Wang, H., Han, Y., Ma, S., Niu, X., Li, N., Shi, C., Qiu, Z., Zhou, H., Bai, Y., and Chen, Q. (2021). Synergistic Effects of Eu-MOF on Perovskite Solar Cells with Improved Stability. *Adv. Mater.* 33, 2102947.
21. Zhumekenov, A. A., Burlakov, V. M., Saidaminov, M. I., Alofi, A., Haque, M. A., Turedi, B., Davaasuren, B., Dursun, I., Cho, N., El-Zohry, A. M., De Bastiani, M., Giugni, A., Torre, B., Di Fabrizio, E., Mohammed, O. F., Rothenberger, A., Wu, T., Goriely, A., and Bakr, O. M. (2017). The Role of Surface Tension in the Crystallization of Metal Halide Perovskites. *ACS Energy Lett.* 2, 1782-1788.